

Contents lists available at ScienceDirect

Wave Motion

journal homepage: www.elsevier.com/locate/wamot





Linear propagation of tsunami and acoustic–gravity waves on a sphere: Geometrical focusing and defocusing

Byron Williams ^a, Ali Abdolali ^{b,c}, Usama Kadri ^a, ^a

- ^a School of Mathematics, Cardiff University, Cardiff, CF24 4AG, UK
- b US Army Engineer Research and Development Center, Coastal and Hydraulics Laboratory, Vicksburg, 39180, MS, USA
- ^c Earth System Science Interdisciplinary Center (ESSIC), University of Maryland, College Park, 20740, MD, USA

ARTICLE INFO

Keywords: Tsunami Acoustic–gravity wave Propagation on a sphere

ABSTRACT

This study investigates the propagation of tsunami and acoustic–gravity waves at oceanic scales, accounting for the Earth's curvature within a linear, potential flow framework. While local, near-field analyses often neglect Earth's curvature and employ Cartesian or cylindrical coordinate systems, this work utilises spherical coordinates to examine wave behaviour over large distances. The analysis reveals that wave amplitudes experience a defocusing effect as they travel from the source (e.g., the Pole) toward the equator, followed by a focusing effect as they approach the antipodal point beyond the equator. A qualitative comparison is made with the 2022 Hunga Tonga–Hunga Ha'apai volcanic eruption in the South Pacific. The study models surface-gravity (tsunami) waves propagating through a compressible water layer, as well as atmospheric acoustic–gravity waves propagating through the air. The entire analysis is carried out within the framework of linear theory.

1. Introduction

The seminal work by Yamamoto [1] proposed the use of low-frequency compression-type waves, known as acoustic–gravity waves, as potential precursors for tsunamis generated by submarine earthquakes. In the ocean, these waves propagate at the speed of sound in water, approximately 1500 m/s, significantly faster than the maximum phase speed of a tsunami. As such, they can carry valuable information about the source event which, if analysed in real time, could provide early insight into the size of the resulting tsunami. However, the solution presented by Yamamoto [1], and subsequently by others, was formulated in integral form and limited to one dimension, which made practical application of the concept challenging.

To address this, Mei and Kadri [2] employed slender body theory to derive an analytical solution that links the geometry and dynamics of an effective seabed uplift with the resulting three-dimensional pressure field. This work was later extended by Williams et al. [3] to also account for the tsunami itself. Because the solution is analytical, the associated inverse problem, determining key fault parameters from pressure recordings, was also solved in a relatively straightforward manner [4].

Building on this foundation, Kadri et al. [5] developed an operational software package that incorporates these analytical models along with machine learning algorithms. The analytical formulation enables sufficiently fast computations for real-time implementation, as demonstrated in [5]. Nonetheless, a key limitation remains: the validity of the results is currently restricted to near-field sources. In several foundational studies, a Cartesian coordinate system has been employed [1,2,6,7]. The axes are unbounded and the origin is typically located either at the seabed or at the unperturbed liquid surface. In setting up such a Cartesian

E-mail address: kadriu@cardiff.ac.uk (U. Kadri).

^{*} Corresponding author.

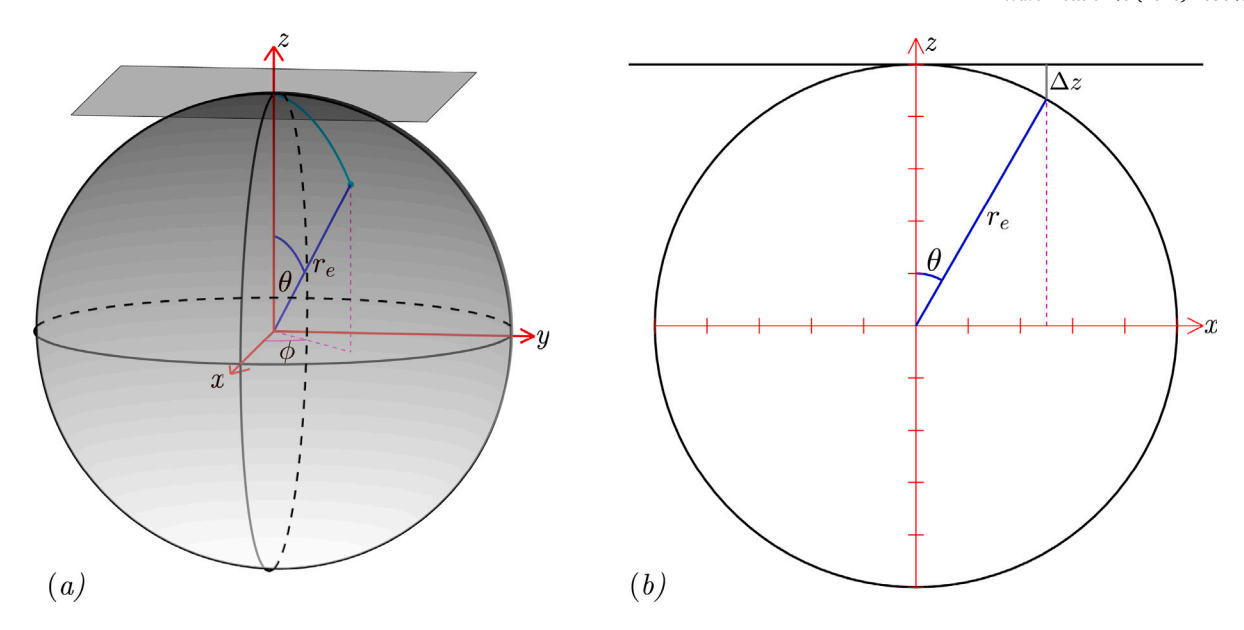


Fig. 1. A tangent plane can approximate spherical geometry locally over a limited range. (a) A sphere with radius r_e and a tangent plane incident at (x, y, z) = (0, 0, 1). The length of the cyan arc in the figure is given by $r_e\theta$ where θ is the polar angle and ϕ is the azimuthal angle. (b) Cross-section through x-z plane. The Δz represents the difference between the tangent approximation and the actual curved surface.

coordinate system one assumption made is that a tangent plane to the sphere will remain a close approximation over the area of interest — see Fig. 1.

If Δz in Fig. 1 is taken as a measure of error between the tangent plane approximation and the actual curved surface, then it is possible to derive a coarse value for how far a geodesic on the surface of the sphere can be travelled before the error exceeds some specified limit, for example 1% (which corresponds to $\Delta Z = 0.01$). Taking the Earth's radius $r_e = 6371$ km [8] the arc length from the point of tangency [(0,1) in the x-z plane] to the 1% error point is given by

$$L = r_e \theta = r_e \left[\frac{\pi}{2} - \tan^{-1} \left(\frac{1 - \Delta Z}{\sqrt{1 - (1 - \Delta Z)^2}} \right) \right] = 901.7 \,\text{km}.$$
 (1.1)

Thus, in the study of long-range propagation of acoustic–gravity waves and tsunamis, a deviation 1% from Cartesian is apparent after travelling approximately 900 km from the source. In addition, the error does not increase linearly with the distance travelled. For propagation in large bodies of water, such as the Pacific Ocean, these errors may be significant. To examine some of the consequences of moving to a global framework, where the Earth is modelled as a rigid sphere supporting a thin fluid layer of constant depth which represents either the ocean or the atmosphere, we employ spherical coordinates and solve the wave equation in these coordinates. The objective is to apply a correction due to Earth curvature to the propagation of tsunami and acoustic–gravity waves at oceanic scales, to be assessed in real-time. Thus, certain simplifications are necessary to allow cost-effective computations. These include approximations related to Earth's elasticity, bathymetry, density and temperature variations in both air and water, as well as the neglect of nonlinear effects. The validity and limitations of these simplifications are further discussed in Section 4.2. Note that, without loss of generality, the analysis is primarily conducted with reference to the ocean as the fluid layer, while the atmospheric case is addressed only when relevant.

Two different length scales, corresponding to two regimes, in the near and far fields, are considered. In the near-field, also referred to as the inner region (see Fig. 2b), we adopt the water depth h as the characteristic length scale. In this regime, the Earth's curvature is neglected, and we consider the generation of acoustic–gravity waves and the tsunami due to an uplifting cylinder. For the near-field view we can use axisymmetric cylindrical coordinates as studied in [9]. In the far-field, also referred to as outer region, we take the radius of the Earth r_e as the reference length scale. At the interface between the near-field and far-field regions, both the value and first derivative, of the velocity function on either side of the interface must match. These matching conditions are sufficient to establish the unknowns of the equations and admit a full solution.

The amplitude of the acoustic–gravity waves and tsunami undergo a modulation governed by the envelope of the theta function $\Theta(\theta)$. This function determines the degree of geometrical defocusing (i.e., attenuation) dependent upon how far around the spherical body the wave has travelled. For example, for a wave originating at the north pole, maximum defocusing occurs at the vicinity of the equator. Continued travel beyond the equator towards the south pole would then see a focusing effect as evidenced in [10]. Reflections, at or near, the poles have not been considered in this work. The envelope itself can be described by a modified form of Bernstein's equation, which is discussed in Section 4.

It should be noted that although we are working at a global scale in this study, we have not taken into account tidal effects. For acoustic–gravity waves, this should not pose a problem since their speeds are much greater than those of tides. However, for completeness, tidal effects should be included.

2. Formulation

The fluid layer is considered inviscid, homogeneous, of constant depth h, residing in a gravitational field of constant magnitude $g=9.81~{\rm m~s^{-2}}$. The layer is supported by a rigid, solid, homogeneous, and isotropic sphere of fixed radius r_e . Spherical coordinates (r,θ,ϕ) are employed, with the origin of coordinates taken to be the centre of the sphere (see Fig. 1a). The radial coordinate is denoted by r, the polar coordinate by θ , and the azimuthal coordinate by ϕ . Assuming irrotational flow the problem is expressed in terms of a velocity potential function for the liquid φ . We make use of linearised, irrotational flow for the liquid. A representation of the flow domain is given in Fig. 1a. Taking into account the compressibility of the fluid – albeit small in the case of the water layer – and neglecting the gravitational potential term, $g\varphi_z$, the velocity potential is governed by the wave equation [11]

$$\nabla^{2} \varphi - \frac{1}{c^{2}} \frac{\partial^{2} \varphi}{\partial t^{2}} = 0, \quad r_{e} \le r \le r_{e} + h, \quad 0 \le \theta \le \pi, \quad 0 \le \phi \le 2\pi, \quad t \ge 0,$$
(2.2)

where c is the speed of sound in the fluid layer. When the Laplacian for spherical coordinates is applied the wave equation becomes

$$\frac{\partial^2 \varphi}{\partial r^2} + \frac{2}{r} \frac{\partial \varphi}{\partial r} + \frac{1}{r^2 \sin(\theta)} \frac{\partial}{\partial \theta} \left(\sin(\theta) \frac{\partial \varphi}{\partial \theta} \right) + \frac{1}{r^2 \sin^2(\theta)} \frac{\partial^2 \varphi}{\partial \phi^2} - \frac{1}{c^2} \frac{\partial^2 \varphi}{\partial t^2} = 0, \tag{2.3}$$

subject to boundary conditions. Following the derivations given in [12], at the free surface we have the combined kinematic and dynamic boundary condition

$$\frac{\partial^2 \varphi}{\partial t^2} + g \frac{\partial \varphi}{\partial r} = 0, \quad r = r_e + h. \tag{2.4}$$

At the rigid seabed (inner and outer regions) the radial component of velocity in the fluid layer is zero

$$\frac{\partial}{\partial r}\varphi(r,\theta,\phi,t)\bigg|_{r=r} = 0. \tag{2.5}$$

Since ϕ is an angular coordinate, solutions should be single-valued, i.e., unchanged as $\phi \to \phi + 2\pi$

$$\varphi(r,\theta,\phi,t) = \varphi(r,\theta,\phi+2\pi,t). \tag{2.6}$$

The rupture in the seabed is modelled in the same way as in [9]. The model consists of a transient, uniform vertical uplift with a circular cross-section located at the seabed where the spherical coordinate $\theta=0$ (i.e., the north pole of the sphere) — see Fig. 2. There is no loss of generality in choosing the North Pole as the origin of the rupture since any other location on the sphere can be reached with a single rotation. Located immediately outside of the rising cylinder we have an annulus between radii R_c (the wall of the cylinder) and R_0 . This annulus is designated the inner region and is made large enough to ensure the evanescent waves arising from the rupture have decayed away, but not so large as to introduce curvature errors.

3. Solutions

3.1. Short-range inner region

The tsunami will travel at speed \sqrt{gh} , with time scale $\sqrt{h/g}$ and length scale h. The acoustic–gravity waves will propagate with velocity c, time scale h/c, and length scale h. Let $\xi = \sqrt{gh}/c$ be a dimensionless parameter that quantifies the influence of gravity relative to compressibility, representing the ratio of gravity wave speed to sound wave speed. Then with hat circumflex denoting non-dimensional parameters the wave equation (2.3) becomes

$$\frac{\partial^2 \hat{\varphi}}{\partial \hat{r}^2} + \frac{2}{\hat{r}} \frac{\partial \hat{\varphi}}{\partial \hat{r}} + \frac{1}{\hat{r}^2 \sin \theta} \frac{\partial}{\partial \theta} \left(\sin \theta \frac{\partial \hat{\varphi}}{\partial \theta} \right) + \frac{1}{\hat{r}^2 \sin^2 \theta} \frac{\partial^2 \hat{\varphi}}{\partial \phi^2} - \xi^2 \frac{\partial^2 \hat{\varphi}}{\partial \hat{r}^2} = 0. \tag{3.7}$$

In the limit as $\xi \to 0$ (i.e., $c \to \infty$), the last term in the wave equation (3.7) becomes negligible and the equation reduces to the incompressible Laplace equation, which is acceptable when analysing pure surface-gravity waves in the ocean. Now let $h/r_e = \epsilon \ll 1$, and $r = r_e + Z$, with $0 \le Z \le h$, then the non-dimensional forms become

$$\hat{r} = \frac{1}{\epsilon} + \hat{Z}, \quad \hat{Z} = \frac{Z}{h}. \tag{3.8}$$

Substituting (3.8) in the wave equation (3.7) gives

$$\frac{\partial^2 \hat{\varphi}}{\partial \hat{Z}^2} + 2\epsilon \frac{\partial \hat{\varphi}}{\partial \hat{Z}} + \frac{\epsilon^2}{\sin \theta} \frac{\partial}{\partial \theta} \left(\sin \theta \frac{\partial \hat{\varphi}}{\partial \theta} \right) + \frac{\epsilon^2}{\sin^2 \theta} \frac{\partial^2 \hat{\varphi}}{\partial \phi^2} - \xi^2 \frac{\partial^2 \hat{\varphi}}{\partial \hat{t}^2} = 0. \tag{3.9}$$

For small θ (near-field solution), we have

$$\frac{\partial^2 \hat{\varphi}}{\partial \hat{Z}^2} + 2\epsilon \frac{\partial \hat{\varphi}}{\partial \hat{Z}} + \frac{\epsilon^2}{\theta} \frac{\partial \hat{\varphi}}{\partial \theta} + \epsilon^2 \frac{\partial^2 \hat{\varphi}}{\partial \theta^2} + \frac{\epsilon^2}{\theta^2} \frac{\partial^2 \hat{\varphi}}{\partial \phi^2} - \xi^2 \frac{\partial^2 \hat{\varphi}}{\partial \hat{t}^2} = 0. \tag{3.10}$$

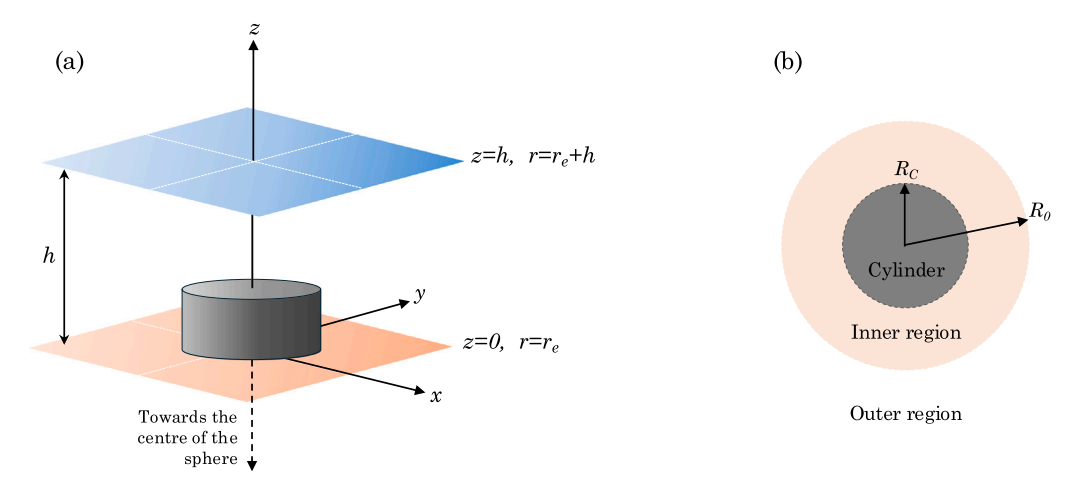


Fig. 2. Representation of the seabed rupture as an uplifting cylinder of radius R_c . Surrounding the cylinder is an annulus of outer radius R_0 . Solutions involve matching function values and first derivatives of the velocity potential at R_0 . (a) Uniform cylindrical uplift at the seabed of a compressible ocean of constant depth h. (b) Top view of rupture regions. The black disc is the uplifting cylinder, the surrounding grey annulus is the inner region, and everything outside of it at radius larger than R_0 is referred to as the outer region.

Here $\theta \ll 1$, but not ϕ . From Fig. 1a we see that the arc length from the north pole is given by $R = \theta r_e$. For small θ we have $\sin(\theta) \approx \theta$, $\theta = R/r_e \equiv \epsilon \hat{R}$ with $\hat{R} = R/h$ being the arc length scaled to the fluid layer thickness. Thus

$$\frac{\partial^2 \hat{\varphi}}{\partial \hat{Z}^2} + 2\epsilon \frac{\partial \hat{\varphi}}{\partial \hat{Z}} + \frac{1}{\hat{R}} \frac{\partial \hat{\varphi}}{\partial \hat{R}} + \frac{\partial^2 \hat{\varphi}}{\partial \hat{R}^2} + \frac{1}{\hat{R}^2} \frac{\partial^2 \hat{\varphi}}{\partial \hat{\varphi}^2} - \xi^2 \frac{\partial^2 \hat{\varphi}}{\partial \hat{t}^2} = 0.$$
(3.11)

For waves propagating in the water layer, where $gh/c^2 \sim (h/r_e)^{1/2}$, we can express $\xi^2 = \mathcal{O}(\epsilon^{1/2})$. Conversely, for atmospheric propagation, $\xi = \mathcal{O}(1)$. Assuming axisymmetric propagation, we set $\partial/\partial\phi = 0$. Thus, to leading order in ϵ , the near-field solution reduces to symmetric cylindrical coordinates

$$\frac{\partial^2 \hat{\varphi}}{\partial \hat{Z}^2} + \frac{1}{\hat{R}} \frac{\partial \hat{\varphi}}{\partial \hat{R}} + \frac{\partial^2 \hat{\varphi}}{\partial \hat{R}^2} - \xi^2 \frac{\partial^2 \hat{\varphi}}{\partial \hat{r}^2} = 0, \tag{3.12}$$

along with the boundary conditions. At the surface

$$\frac{\partial^2 \hat{\varphi}}{\partial \hat{r}^2} + \frac{\partial \hat{\varphi}}{\partial \hat{z}} = 0. \tag{3.13}$$

At the seabed there is a no-penetration condition (the vertical velocity is zero):

$$\frac{\partial \hat{\varphi}}{\partial \hat{\mathcal{T}}} = \hat{W}_0(\hat{R}, \hat{t}),\tag{3.14}$$

where \hat{W}_0 is the vertical velocity of the cylinder given by

$$\hat{W}_0 = \frac{\zeta_0}{2} \mathcal{H} \left(\hat{R}_c^2 - \hat{R}^2 \right) \mathcal{H} \left(\hat{t} (\hat{\tau} - \hat{t}) \right), \tag{3.15}$$

where ζ_0 is the final vertical displacement of the cylinder, \mathcal{H} is the Heaviside function, and $\hat{\tau}$ is the duration of the vertical motion. The continuity conditions between the inner and outer regions are given by

$$\hat{\varphi}_{\text{in}}|_{\hat{R}_0} = \hat{\varphi}_{\text{out}}|_{\theta_0 = \epsilon \hat{R}_0}$$
, (3.16)

$$\frac{\partial}{\partial \hat{R}} \hat{\varphi}_{\rm in} \Big|_{\hat{R}_{\rm o}} = \frac{\partial \theta}{\partial \hat{R}} \frac{\partial}{\partial \theta} \hat{\varphi}_{\rm out} = \epsilon \frac{\partial}{\partial \theta} \hat{\varphi}_{\rm out} \Big|_{\hat{\theta}_{\rm o} = \epsilon \hat{R}_{\rm o}}. \tag{3.17}$$

The point at which the matching takes place in the continuity equations is R_0 on the LHS of the continuity equations where $\hat{\varphi} = \hat{\varphi}_{in}(\hat{R},\hat{Z},\hat{t})$ and its equivalent $\theta_0 = \epsilon \hat{R}_0$ on the RHS where $\hat{\varphi}_{out} = \hat{\varphi}_{out}(\hat{t},\theta)$.

The velocity potential $\hat{\varphi}_{in}$ appearing in the continuity conditions is already known in integral form from [9] and will be referenced in the following text as the cylindrical solution:

$$\begin{aligned} & \varphi_{in}(\mathbf{R}, \mathbf{Z}, t) = \\ & 4\hat{R}_c \hat{W}_0 \int_0^\infty \frac{\hat{\mu}_0 \cosh(\hat{\mu}_0 \hat{Z}) \sin(\hat{\omega}\hat{\tau}/2)}{\hat{\omega}\hat{q}_0 \left[\sinh(2\hat{\mu}_0) + 2\hat{\mu}_0 \right]} \left[Y_0(\hat{q}_0 \hat{R}) \cos\left(\hat{\omega}\hat{t} - \frac{\hat{\omega}\hat{\tau}}{2}\right) - J_0(\hat{q}_0 \hat{R}) \sin\left(\hat{\omega}\hat{t} - \frac{\hat{\omega}\hat{\tau}}{2}\right) \right] J_1(\hat{q}_0 \hat{R}_c) d\hat{\omega} \\ & + 4\hat{R}_c \hat{W}_0 \sum_{n=1}^\infty \int_{\hat{\omega}_n}^\infty \frac{\hat{\mu}_n \cos(\hat{\mu}_n \hat{Z}) \sin(\hat{\omega}\hat{\tau}/2)}{\hat{\omega}\hat{q}_n \left[\sin(2\hat{\mu}_n) + 2\hat{\mu}_n \right]} \left[Y_0(\hat{q}_0 \hat{R}) \cos\left(\hat{\omega}\hat{t} - \frac{\hat{\omega}\hat{\tau}}{2}\right) - J_0(\hat{q}_n \hat{R}) \sin\left(\hat{\omega}\hat{t} - \frac{\hat{\omega}\hat{\tau}}{2}\right) \right] J_1(\hat{q}_n \hat{R}_c) d\hat{\omega} \end{aligned} \tag{3.18}$$

where $\hat{\mu}_n$ are the eigenvalues and \hat{q}_n are wave numbers, with mode numbers n (n = 0, 1, 2, ...) – that are often omitted for brevity – J_m , Y_m (m = 0, 1) are Bessel functions with subscripts denoting the type of the Bessel function. The first term in (3.18) corresponds to the contribution of the tsunami (the zeroth mode), with μ_0 real and positive. Thus, the potential exponentially decays with depth, as expected. On the other hand, the second term comprises a countable infinity of acoustic modes, with eigenvalues μ_n . Unlike the tsunami, these modes exhibit an oscillatory behaviour across h, while come of them are progressive in space in R, others are evanescent as will be further discussed in the following dispersion relation section.

Note, that there is a Z dependency in the inner region, since the characteristic length scale is h, and thus $\hat{Z} = \mathcal{O}(1)$. On the other hand, for the outer region the characteristic length scale is r_e , i.e., $\Delta Z \equiv h \ll r_e$. Thus the dependency in the Z direction is negligible for the outer region. This miss-match is handled by setting Z = h in the inner region when considering surface waves and integrating over Z in the inner region when considering acoustic–gravity waves.

Assume $\hat{\varphi}(\hat{Z}, \hat{R}, \hat{t}) = \zeta(\hat{Z})\rho(\hat{R})Y(\hat{t})$ and substitute into (3.12) to give, after re-arranging,

$$\frac{1}{\zeta} \frac{\mathrm{d}^2 \zeta}{\mathrm{d}\hat{Z}^2} + \frac{1}{\rho \hat{R}} \frac{\mathrm{d}\rho}{\mathrm{d}\hat{R}} + \frac{1}{\rho} \frac{\mathrm{d}^2 \rho}{\mathrm{d}\hat{R}^2} = \frac{\xi^2}{Y} \frac{\mathrm{d}^2 Y}{\mathrm{d}\hat{r}^2} = \text{constant} \equiv -\hat{k}_s^2, \tag{3.19}$$

$$\implies Y(\hat{t}) = A_1 \cos\left(\frac{\hat{k}_s}{\xi}\hat{t}\right) + A_2 \sin\left(\frac{\hat{k}_s}{\xi}\hat{t}\right),\tag{3.20}$$

with \hat{k}_s a wave-number. From (3.19), and following Hendin and Stiassnie [9] we have

$$\frac{1}{\rho \hat{R}} \frac{\mathrm{d}\rho}{\mathrm{d}\hat{R}} + \frac{1}{\rho} \frac{\mathrm{d}^2 \rho}{\mathrm{d}\hat{R}^2} = -\left(\frac{1}{\zeta} \frac{\mathrm{d}^2 \zeta}{\mathrm{d}\hat{Z}^2} + \hat{k}_s^2\right) = \hat{q}^2,\tag{3.21}$$

where \hat{q}^2 is the separation constant between \hat{R} and \hat{Z} . The separation produces a set of two ODEs,

$$\frac{d^{2}\zeta}{d\hat{Z}^{2}} + (\hat{k}_{s}^{2} + \hat{q}^{2})\zeta = 0, \qquad \frac{d^{2}\rho}{d\hat{R}^{2}} + \frac{1}{\hat{R}}\frac{d\rho}{d\hat{R}} - \hat{q}^{2}\rho = 0.$$
(3.22)

The solution in the \hat{Z} direction is

$$\zeta(\hat{Z}) = B_1 \cos(\hat{\mu}\hat{Z}) + B_2 \sin(\hat{\mu}\hat{Z}), \qquad \hat{\mu} = \sqrt{\hat{k}_s^2 + \hat{q}^2}, \tag{3.23}$$

which is in agreement with Hendin and Stiassnie [9].

The solution in the radial direction is a linear combination of the Bessel functions J_0 and Y_0 [13]

$$\rho(\hat{R}) = C_1 J_0(\hat{i}\hat{q}\hat{R}) + C_2 Y_0(\hat{i}\hat{q}\hat{R}). \tag{3.24}$$

Note that Eq. (3.18) is valid only outside the cylindrical region (see Fig. 2b), requiring that $\hat{R} > \hat{R}_c$. Therefore, in the limit as $\hat{R} \to 0$, we have $\hat{R}_c \to 0$, implying that $\hat{\varphi}_{in} \to 0$. Consequently, the solution becomes valid for all $\hat{R} > \hat{R}_c$.

3.2. Dispersion relation

The dispersion relation can be derived without knowledge of the function $\rho(\hat{R})$. The method shown here utilises Eqs. (3.20) and (3.23), along with $\varphi(\hat{Z}, \hat{R}, \hat{t}) = \zeta(\hat{Z})\rho(\hat{R})Y(\hat{t})$, and reverts back to dimensional quantities for the calculation. Let $A_1, A_2, B_1, B_2, C_1, C_2$ be constants then

$$Y(\hat{t}) = A_1 \cos\left(\frac{\hat{k}_s}{\xi}\hat{t}\right) + A_2 \sin\left(\frac{\hat{k}_s}{\xi}\hat{t}\right) \implies Y(t) = A_1 \cos\left(\omega t\right) + A_2 \sin\left(\omega t\right), \quad \frac{\hat{k}_s}{\xi}\hat{t} = k_s ct = \omega t, \tag{3.25}$$

$$\zeta(\hat{Z}) = B_1 \cos(\hat{\mu}\hat{Z}) + B_2 \sin(\hat{\mu}\hat{Z}) \implies \zeta(Z) = B_1 \cos(\mu Z) + B_2 \sin(\mu Z). \tag{3.26}$$

Application of the boundary conditions for the surface (Z = h) and the bottom boundary condition (Z = 0)

$$\frac{\partial^2 \varphi}{\partial t^2} + g \frac{\partial \varphi}{\partial Z} = 0 \bigg|_{Z=h}, \qquad \frac{\partial \varphi}{\partial z} = 0 \bigg|_{Z=0}, \tag{3.27}$$

results in the dispersion relation

$$\omega^2 = -g\mu \tan(\mu h). \tag{3.28}$$

Rearrangement of the expression for μ from (3.23), and examination of the roots of the dispersion relation (3.28), produces three categories

(i) Single imaginary root
$$\mu = i\mu_0$$
, $\implies q_0 = i|q_0| = i\sqrt{k_s^2 + \mu_0^2} = i\sqrt{\frac{\omega^2}{c^2} + \mu_0^2}$, (3.29)

(ii) Finite number of real roots
$$\mu_n$$
, when $\mu_n^2 < \frac{\omega^2}{c^2}$, $\implies q_n = \mathrm{i}|q_n| = \mathrm{i}\sqrt{\frac{\omega^2}{c^2} - \mu_n^2}$, (3.30)

(iii) Infinite number of real roots
$$\mu_n$$
, when $\mu_n^2 > \frac{\omega^2}{c^2} \implies q_n = \sqrt{\mu_n^2 - \frac{\omega^2}{c^2}}$. (3.31)

Category (i) corresponds to surface-gravity waves (tsunamis), which are progressive in the radial direction R and decay exponentially with depth Z. Category (ii) represents progressive acoustic–gravity modes that are oscillatory in Z. Finally, category (iii) includes evanescent acoustic–gravity modes that decay exponentially in R and can therefore be neglected in far-field (outer region) calculations.

For the tsunami n=0 and acoustic–gravity modes $n=1,\ldots,N$ the wave numbers and q_n are purely imaginary and so the argument of the Bessel functions, in the inner region, becomes real indicating oscillating, progressive modes. When $n=N+1,\ldots\infty,q_n$ is real and in that case we have the modified Bessel functions representing non-progressive evanescent modes. Thus, the expression for the near-field region is in agreement with Hendin and Stiassnie [9], with the solution given by (3.18). In the incompressible limit, $c\to\infty$, the tsunami eigenvalue reduces exactly to the wavenumber, indicating that no correction due to compressibility is present. In this regime, progressive acoustic modes cease to exist, as expected. Conversely, the mathematical limit $c\to0$ corresponds to a vacuum, where the physical problem becomes ill-posed, since neither gravity nor acoustic waves can exist or propagate in such a medium.

3.3. Long range outer region

To tackle the far-field solution re-scale lengths by the characteristic length scale r_e , and time, by the time scale $e^{-1}\sqrt{h/g}$. Now $\bar{r}_e=1$, and $\bar{h}\equiv\mathcal{O}(\epsilon)$. Since $0\leq\bar{Z}\leq\bar{h}$, it follows that $\bar{Z}=\mathcal{O}(\epsilon)$. Under this non-dimensional setting $r=r_e+Z$ becomes $\bar{r}=1+\mathcal{O}(\epsilon)$ and $\partial/\partial\bar{r}=0$. Physically, this means that in the far-field waves only propagate at the surface of earth, i.e., the ocean or the atmosphere has a negligible length compared to the radius of the earth. The small angle approximation is no longer valid in the far-field. Substituting into the wave equation (2.3), whilst maintaining the axial symmetry from the inner region, i.e., $\partial/\partial\bar{\phi}=0$, then to the leading order we obtain

$$\frac{1}{\sin(\theta)} \frac{\partial}{\partial \theta} \left(\sin(\theta) \frac{\partial \bar{\phi}}{\partial \theta} \right) - \xi^2 \frac{\partial^2 \bar{\phi}}{\partial \bar{t}^2} = 0. \tag{3.32}$$

3.4. Constructing the outer solution

Take the function $\bar{\phi} = A\left(\bar{T},\beta\right)\Theta(\theta)\mathrm{e}^{-\mathrm{i}\bar{\phi}\bar{t}}$ where $\bar{T} = \sigma\left(\bar{t} - \bar{\tau}/2\right)$, $\beta = \sigma\theta$ and $\sigma \ll 1$. We seek to demonstrate that the function $A(\bar{T},\beta)$ appearing in the ansatz solution $\bar{\phi}$ to (3.32) is equivalent to the long-range version of the solution for the inner region cylindrical solution which is already known from [9] and appears in (3.18). Since the propagation in the outer-region can be represented as an evolving envelope at the surface of the sphere (i.e., no Z or r dependency) the approach solution for the tsunami and the acoustic–gravity waves would be in principle the same solution. Thus, for the sake of brevity consider only the tsunami (Z = h) contribution from the propagating parts of (3.18), i.e., the first line

$$\bar{\varphi}_{in}(\bar{R},\bar{t}) = 4\bar{R}_c\bar{W}_0 \int_0^\infty \frac{\bar{\mu}_0 \cosh(\bar{\mu}_0\bar{h}) \sin(\bar{\omega}\bar{\tau}/2)}{\bar{\omega}\bar{q}_0 \left[\sinh(2\bar{\mu}_0\bar{h}) + 2\bar{\mu}_0\bar{h} \right]} \left[Y_0(\bar{q}_0\bar{R}) \cos\left(\bar{\omega}\bar{t} - \frac{\bar{\omega}\bar{\tau}}{2}\right) - J_0(\bar{q}_0\bar{R}) \sin\left(\bar{\omega}\bar{t} - \bar{\omega}\bar{\tau}/2\right) \right] J_1(\bar{q}_0\bar{R}_c) d\bar{\omega}. \tag{3.33}$$

Long-range approximations for the Bessel functions in (3.33) can be expressed following equation (10.7.8) of [14] as

$$J_0\left(\bar{q}_0\bar{R}\right) = \sqrt{\frac{2}{\pi\bar{q}_0\bar{R}}}\cos\left(\bar{q}_0\bar{R} - \frac{\pi}{4}\right), \quad Y_0\left(\bar{q}_0\bar{R}\right) = \sqrt{\frac{2}{\pi\bar{q}_0\bar{R}}}\sin\left(\bar{q}_0\bar{R} - \frac{\pi}{4}\right). \tag{3.34}$$

With these approximations substituted into (3.33) along with the trigonometric identity $\sin(X - Y) = \sin(X)\cos(Y) - \cos(X)\sin(Y)$ we have

$$\bar{\varphi}_{in}(\bar{R},\bar{t}) = 4\bar{W}_0\bar{R}_c \int_0^\infty \frac{\bar{\mu}_0 \cosh(\bar{\mu}_0\bar{h}) \sin(\bar{\omega}\bar{\tau}/2)}{\bar{\omega}\bar{q}_0 \left[\sinh(2\bar{\mu}_0\bar{h}) + 2\bar{\mu}_0\bar{h} \right]} \sqrt{\frac{2}{\pi\bar{q}_0\bar{R}}} \sin\left[-\bar{\omega} \left(\bar{t} - \frac{\bar{\tau}}{2} \right) + \bar{q}_0\bar{R} - \frac{\pi}{4} \right] J_1(\bar{q}_0\bar{R}_c) d\bar{\omega}. \tag{3.35}$$

Substitute $\bar{\varphi} = A(\bar{T}, \beta) \Theta(\theta) e^{-i\bar{\omega}\bar{t}}$ into (3.32) to give

$$\sigma\cot(\theta)\Theta\frac{\partial A}{\partial \beta} + \cot(\theta)A\frac{d\Theta}{d\theta} + 2\sigma\frac{\partial A}{\partial \beta}\frac{d\Theta}{d\theta} + A\frac{d^2\Theta}{d\theta^2} + \xi^2\left[2\mathrm{i}\sigma\bar{\omega}\Theta\frac{\partial A}{\partial\bar{T}} + \bar{\omega}^2\Theta A\right] = \mathcal{O}(\sigma^2). \tag{3.36}$$

Collecting leading order terms, and applying the change of variable $w = \cos(\theta)$, (3.36) can be re-written as

$$(1-w^2)\frac{\mathrm{d}^2\Theta}{\mathrm{d}w^2} - 2w\frac{\mathrm{d}\Theta}{\mathrm{d}w} + \xi^2\bar{\omega}^2\Theta = 0. \tag{3.37}$$

This is a Legendre equation which has solutions that are a linear combination of the Legendre functions $P_{\lambda}(w)$ and $Q_{\lambda}(w)$, where λ is the degree of the Legendre function. Thus with E_1, E_2 as integration constants to be determined we have

$$\Theta(w) = E_1 P_{\lambda}(w) + E_2 Q_{\lambda}(w), \quad \lambda = \frac{1}{2} \sqrt{4\xi^2 \bar{\omega}^2 + 1} - \frac{1}{2}, \quad w = \cos(\theta). \tag{3.38}$$

Collecting terms at the next order, $\mathcal{O}(\sigma)$ and after some re-arrangement, we find $\partial A/\partial T$ can be written in terms of $\partial A/\partial \beta$ as follows

$$\frac{\partial A}{\partial \bar{T}} = i \frac{\cot(\theta)\theta + 2\partial\theta/\partial\theta}{2\xi^2\bar{\omega}\theta} \frac{\partial A}{\partial\theta}.$$
(3.39)

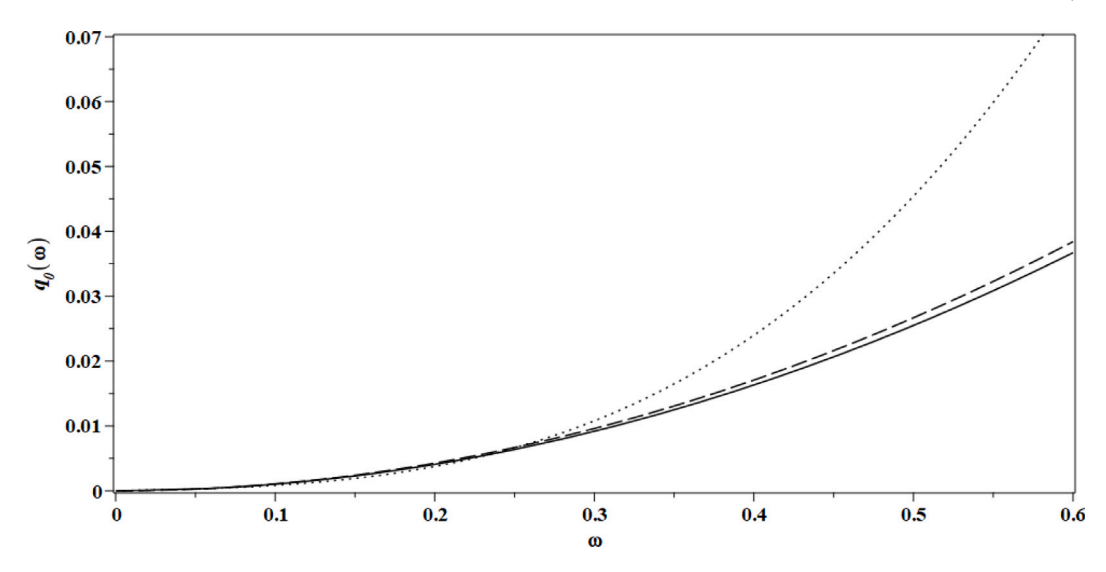


Fig. 3. Plots of $q_0(\omega)$, using the full dispersion relation (solid line); Eq. (3.44) (dashed line); approximate expression (3.45) derived in [15] (dotted line).

The equation $\partial A/\partial \bar{T} = i\partial A/\partial \beta$ has solutions of the form $A(\bar{T},\beta) = f(i\bar{T}+\beta)$, where f is some arbitrary function. The solution of (3.39) is of the form

$$A(\bar{T}, \beta) = f(x), \quad x \equiv \left(i\frac{\cot(\theta)\Theta + 2\partial\Theta/\partial\theta}{2\mathcal{E}^2\bar{\omega}\Theta}\bar{T} + \beta\right),\tag{3.40}$$

and again f(x) is some arbitrary function. Let

$$\begin{split} P_{\lambda_0} &= P_{\lambda}(\cos\theta_0), \quad Q_{\lambda_0} = Q_{\lambda}(\cos\theta_0), \quad P_{\lambda_0+1} = P_{\lambda+1}(\cos\theta_0), \quad Q_{\lambda_0+1} = Q_{\lambda+1}(\cos\theta_0), \\ P_{\lambda} &= P_{\lambda}(\cos\theta), \qquad Q_{\lambda} = Q_{\lambda}(\cos\theta), \qquad P_{\lambda+1} = P_{\lambda+1}(\cos\theta), \qquad Q_{\lambda+1} = Q_{\lambda+1}(\cos\theta), \end{split} \tag{3.41}$$

with

$$\frac{\partial \Theta}{\partial \theta} = \frac{(\lambda + 1)\sin(\theta)}{\cos^2(\theta) - 1} \left[E_1 \left(\cos(\theta) P_{\lambda} - P_{\lambda + 1} \right) + E_2 \left(\cos(\theta) Q_{\lambda} - Q_{\lambda + 1} \right) \right]. \tag{3.42}$$

Then the sine term with square brackets in (3.35) can be written in the form $f(x) = \sin[ax+b]$ with $a = \bar{q}_0/\sigma$ and $b = -\pi/4$. Assuming that $\bar{\tau} \ll \bar{t}$, reverting from (\bar{T}, β) to $(\sigma \bar{t}, \sigma \theta)$ we obtain

$$\frac{\bar{q}_0}{\sigma} \left[i \frac{\cot(\theta)\Theta + 2\partial\Theta/\partial\theta}{2\xi^2 \bar{\omega}\Theta} \right] \sigma \bar{t} = -\bar{\omega}\bar{t}, \quad \text{and} \quad \frac{\bar{q}_0}{\sigma}(\sigma\theta) = \bar{q}_0 \bar{R}. \tag{3.43}$$

From (3.29), ($\sigma \neq 0$), and with \bar{q}_0 numerically positive (so we are able to drop the magnitude bars) we have

$$\bar{q}_0(\bar{\omega}) = \frac{2\xi^2 \Theta}{\cot(\theta)\Theta + 2\bar{\partial}\Theta/\bar{\partial}\theta} \bar{\omega}^2, \qquad \bar{R} = \theta. \tag{3.44}$$

In what follows, we revert to the dimensional formulation. As numerical verification of the relationship between q_0 and ω in (3.44), Fig. 3 compares values for q_0 obtained from solving the dispersion relation at the matching point θ_0 , against values given by (3.44) and an approximate expression from [15] (equation number 5.33) and written here as (3.45).

$$q_0 = \frac{\omega}{\sqrt{gh}} \left(1 + \frac{\omega^2 h}{6g} \right). \tag{3.45}$$

The values for q_0 obtained from (3.44) remain close to the dispersion relation solution as far as $\omega = 0.6\,\mathrm{rads}^{-1}$. Thus, φ_{out} can now be written as

$$\varphi_{out}(t,\theta) = A(R,t) \left[E_1 P_{\lambda} + E_2 Q_{\lambda} \right] e^{-i\omega t}, \quad R = \theta r_{\sigma}$$
 (3.46)

where A(R, t) can be written following (3.35) since we require equality at the interface between inner and outer regions.

3.5. Continuity between inner and outer regions

The initial conditions are determined by the particular rupture conditions studied. The near-field solution is given by (3.18), which is assumed to be the source of the velocity potential. Matching at R_0 then ensures a smooth transition between the cylindrical

solution of the inner region and the long-range spherical coordinates of the outer region. The velocity potential functions on either side of R_0 must match in both value and first derivative at R_0

$$\varphi_{in}(R,t)\big|_{R_0} = \left.\varphi_{out}(t,\theta)\right|_{\theta_0 = \frac{R_0}{\tau}},\tag{3.47}$$

$$\frac{\partial}{\partial R}\varphi_{in}(R,t)\bigg|_{R_0} = \frac{1}{r_e} \frac{\partial}{\partial \theta}\varphi_{out}(t,\theta)\bigg|_{\theta_0 = \frac{R_0}{r_o}}.$$
(3.48)

3.6. Determining the unknown constants

The known velocity potential $\varphi_{in}(R,t)$ for the inner region now has to satisfy the continuity conditions (3.47) and (3.48) with the outer region. The matching is carried out at a distance R_0 from the centre of the cylinder and at time $t_0 = R_0/\sqrt{gh}$ (the arrival time of the tsunami at the distance R_0). The actual value chosen for R_0 is a compromise between being far enough away from the rising cylinder in order for the evanescent waves to decay away, while not being so far as to introduce curvature issues — see (1.1) for the upper limit. Allowing a distance of five times the water depth (5h km) for evanescent wave decay, in addition to the cylinder radius (R_c km) gives the lower limit (5h + R_c). Therefore R_0 km is chosen to satisfy these constraints. Increasing this radius up to the upper limit of (1.1) would retain the inner solution for longer before the defocusing effects begin. Conversely decreasing the radius would begin the defocusing earlier. Given the radius of the earth, the overall effect of relocating R_0 on defocusing/ focusing would be negligible.

The first continuity condition gives

$$\Phi \equiv \varphi_{in}(R_0, t_0) = A(t_0, R_0) \left[E_1 P_{\lambda_0} + E_2 Q_{\lambda_0} \right] e^{-i\omega t_0}, \quad \theta_0 = \frac{R_0}{r_e}.$$
(3.49)

The second continuity condition then gives

$$\Phi_{R} \equiv \frac{\partial}{\partial R} \varphi_{in} \Big|_{t_{0}, R_{0}} = \frac{\partial \theta}{\partial R} \frac{\partial}{\partial \theta} \varphi_{out} \Big|_{t_{0}, \theta_{0}}, \quad \frac{\partial \theta}{\partial R} = \frac{1}{r_{e}}.$$
(3.50)

To obtain the left-hand side of (3.50) differentiate (3.33) with respect to R to give

$$\Phi_R = 4R_cW_0\int_0^\infty \frac{\mu_0\cosh(\mu_0h)\sin(\omega\tau/2)}{\omega\left[\sinh(2\mu_0h) + 2\mu_0h\right]} \left[-Y_1(q_0R_0)\cos\left(\omega t_0 - \frac{\omega\tau}{2}\right) + J_1(q_0R_0)\sin\left(\omega t_0 - \frac{\omega\tau}{2}\right) \right] J_1(q_0R_c)\mathrm{d}\omega. \tag{3.51}$$

To obtain the right-hand side of (3.50) use

$$\frac{1}{r_e} \frac{\partial}{\partial \theta} \varphi_{out} \Big|_{t_0, \theta_0} = \frac{1}{r_e} \frac{\partial}{\partial \theta} \left\{ \sigma \frac{\partial}{\partial \beta} A(T, \beta) \left[E_1 P_{\lambda_0} + E_2 Q_{\lambda_0} \right] + A(T, \beta) \frac{(\lambda + 1) \sin(\theta_0)}{\cos^2(\theta_0 - 1)} \left[E_1 \cos(\theta_0) P_{\lambda_0} + E_2 \cos(\theta_0) Q_{\lambda_0} - E_1 P_{\lambda_0 + 1} - E_2 Q_{\lambda_0 + 1} \right] \right\} e^{-i\omega t}$$
(3.52)

Eqs. (3.49), (3.50) form a set of simultaneous equations in unknowns E_1 and E_2 which can be solved to give

$$E_{1} = -\frac{\left(\left(-\boldsymbol{\Phi}(\lambda+1)\boldsymbol{Q}_{\lambda_{0}+1} + \boldsymbol{Q}_{\lambda_{0}}\left(\boldsymbol{\Phi}(\lambda+1)\cos\left(\theta_{0}\right) + \sin\left(\theta_{0}\right)\boldsymbol{r}_{e}\boldsymbol{\Phi}_{R}\right)\right) - \sin\left(\theta_{0}\right)\boldsymbol{r}_{e}\boldsymbol{\Phi}_{R}\boldsymbol{Q}_{\lambda_{0}}\right)e^{\mathrm{i}\omega t_{0}}}{\boldsymbol{\Phi}(\lambda+1)\left(\boldsymbol{P}_{\lambda_{0}}\boldsymbol{Q}_{\lambda_{0}+1} - \boldsymbol{Q}_{\lambda_{0}}\boldsymbol{P}_{\lambda_{0}+1}\right)},$$
(3.53)

$$E_{2} = \frac{\left(\left(-\boldsymbol{\Phi}\left(\lambda+1\right)P_{\lambda_{0}+1} + P_{\lambda_{0}}\left(\boldsymbol{\Phi}\left(\lambda+1\right)\cos\left(\theta_{0}\right) + \sin\left(\theta_{0}\right)r_{e}\boldsymbol{\Phi}_{R}\right)\right) - \sin\left(\theta_{0}\right)r_{e}\boldsymbol{\Phi}_{R}P_{\lambda_{0}}\right)e^{\mathrm{i}\omega t_{0}}}{\boldsymbol{\Phi}\left(\lambda+1\right)\left(P_{\lambda_{0}}Q_{\lambda_{0}+1} - Q_{\lambda_{0}}P_{\lambda_{0}+1}\right)},\tag{3.54}$$

with E_1 and E_2 now determined (3.46) can be reduced by cancellation of the $e^{\pm i\omega t_0}$ terms to

$$\varphi_{out}(t,\theta) = A(R,t) \left[E_1 P_{\lambda} + E_2 Q_{\lambda} \right], \quad R = \theta r_e. \tag{3.55}$$

Note that it is not necessary to assign numerical values to σ since the terms cancel out during the derivations. Taking the fluid density to be ρ , the surface elevation and dynamic pressure can be derived from

$$\eta = -\frac{1}{g} \frac{\partial}{\partial t} \varphi_{out}(t, \theta), \qquad P = -\rho \frac{\partial}{\partial t} \varphi_{out}(t, \theta). \tag{3.56}$$

4. Results and discussion

Many studies of tsunami and acoustic–gravity wave propagation use Cartesian or cylindrical coordinates. However, the curvature of the Earth unavoidably introduces errors for points far removed from the source. In this paper, we have considered an axially symmetric rupture occurring at the north pole and studied the propagation over the surface of the sphere. The Earth system is modelled as a thin fluid layer of constant depth overlying a rigid sphere, facilitating real-time tsunami assessment through acoustic–gravity waves in the ocean or atmosphere. Consequently, the solution must be computationally efficient.

Table 1
Constants and parameters used in surface elevation comparison of Fig. 5.

Constant	Description	Value
g	Acceleration due to gravity	9.81 m s ⁻²
r_e	Radius of earth	6371 km
R_c	Radius of cylindrical rupture	40 km
R_0	Radius of inner region	120 km
c	Speed of sound in water	1500 m s^{-1}
W_0	Uplift velocity	0.1 m s^{-1}

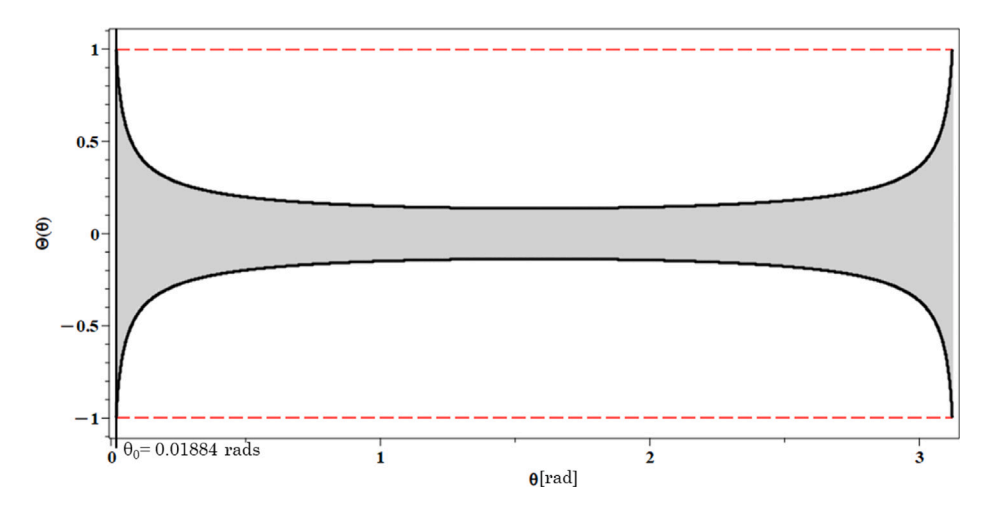


Fig. 4. Plot of theta function (3.38) (grey), upper and lower limits ± 1 (red), and approximate envelope function (4.57) (black). North pole (rupture origin) is located at $\theta=0$, matching point at $\theta=\theta_0=R_0/R_e=0.01884$, maximum defocusing occurs at $\theta=\pi/2$, antipodal matching point is at $\theta=\pi-\theta_0$, and the South pole is at $\theta=\pi$. (For interpretation of the references to colour in this figure legend, the reader is referred to the web version of this article.)

To achieve this goal we split our studies into two regions (inner and outer) with different scales in each. By employing a suitable scaling for the inner region (the near-field), we were able to show that the situation is exactly analogous to that studied in an earlier work [9]. This correspondence allowed us to take an established integral solution (3.18) as our desired initial velocity potential, valid for the region outside of the uplifting cylinder, but within some arbitrary radius R_0 . The radius R_0 is chosen to be far enough from the rupture for the evanescent waves to decay, though close enough so that curvature effects can be ignored. In the studied numerical examples a value of 120 km is taken to satisfy these requirements.

For the outer region $(R > R_0)$ the scaling was changed to reflect the reference length scale switching from h to r_e thus providing a far-field perspective. We found that the amplitude derived in the cylindrical solution is multiplied by $\Theta(\theta)$ when moving to the spherical case. The function $\Theta(\theta)$ governs the defocusing/focusing behaviour of the wave-forms due to the spherical geometry involved. The action of $\Theta(\theta)$ is as follows: $\Theta(\theta)$ begins with a value of 1 at θ_0 since the amplitudes of the cylindrical solution and the spherical solution must match at this radius. Then, as θ increases, we see a decrease in amplitude (defocusing) as θ approaches $\pi/2$. From this point $\Theta(\theta)$ begins to increase in magnitude (focusing effect) until the value of 1 is again attained at $\theta = \pi - \theta_0$.

Since $\Theta(\theta)$ multiplies the cylindrical solution then the amplitude of the cylindrical solution is modulated by $\Theta(\theta)$ as the waves propagate over the surface of the sphere, first defocusing as they approach the equator $\theta = \pi/2$, and then focusing again as they near the South pole $\theta = \pi$. The acoustic-gravity waves resulting from the second term in (3.18), would undergo similar defocusing/focusing. A plot of $\Theta(\theta)$ is shown in Fig. 4. Note that $\Theta(\theta)$ is only valid in the range $\theta_0 \le \theta \le (\pi - \theta_0)$. If calculations are carried out using the outer velocity potential for distances not falling within this range, then amplification of the surface elevation can be reported. The function $\Theta(\theta)$ applies to any disturbance whose source aligns with the scaling assumptions used in the derivation. Accordingly, we present amplitude corrections for waves originating from a cylindrical source, from fault ruptures (both rectangular and 2D transect representations). Some of these waves are derived directly from our analytical formulation, while others come from numerical simulations that are then adjusted using $\Theta(\theta)$. Detailed information on the numerical model is provided in Appendix A.

The envelope governing the changing magnitude of $\Theta(\theta)$ can be closely approximated by a modified form of a result found in [16] and attributed to Bernstein. The modification involves a re-scaling of Bernstein's original result by a constant K:

$$|\Theta(\theta)| \le K\sqrt{\frac{2}{\pi\lambda}} \left(1 - \cos^2\theta\right)^{-\frac{1}{4}}, \qquad K = \sqrt{\frac{\pi\lambda}{2}} \left(1 - \cos^2\theta_0\right)^{\frac{1}{4}}. \tag{4.57}$$

The black traces in Fig. 4 were obtained with (K = 8.68). As a numerical example, we take those parameters listed in Table 1 which reproduce Figure 5.2 from [9]. The aim is to compile a side-by-side comparison of the tsunami contribution of the cylindrical

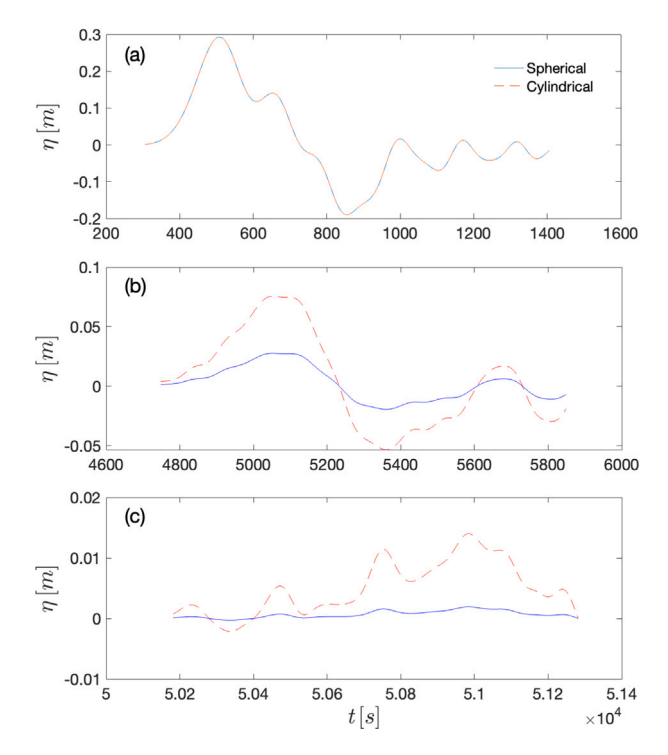


Fig. 5. Comparison between the surface elevation from (3.18), against (3.56) which uses spherical coordinates. Cylindrical solution is a red dash trace, whereas spherical solution is a blue solid trace. (a) Distance from source 120 km. This is the matching point. (b) Distance from source 1000 km as in [9] (c) Distance from source 10000 km. Near the maximum defocusing point. (For interpretation of the references to colour in this figure legend, the reader is referred to the web version of this article.)

solution, against the solution for η generated by (3.56), which utilises spherical coordinates. Comparisons are made at three distances from the source, namely 120 km (the matching point), 1000 km (as in Figure 3 of Hendin and Stiassnie [9]), and 10 000 km (which corresponds to $\theta \approx \pi/2$). The resulting surface elevation wave-forms are found in Fig. 5.

4.1. Energy considerations

A heuristic argument can be made to explain the form of the theta function envelope (4.57) based on energy considerations. In a circular wavefront, the energy of the wave spreads out as the wave travels away from the source. For a circular wavefront, the wavefront is an expanding circle in two dimensions. As the wave travels outward, the circumference of the circle increases, which means the energy is spread over a larger area. The energy density decreases as the wavefront expands. Since the total energy is conserved (assuming no losses), the energy density which is proportional to the square of the amplitude, is inversely proportional to the circumference of the circle, i.e., $\eta^2 \propto [2\pi r_e \sin(\theta)]^{-1}$. Thus $\eta \propto (1-\cos^2(\theta))^{-1/4}$ which is in agreement with (4.57).

4.2. Assumptions/limitations

Having described the spherical solution, (3.55), some of the underlying assumptions and limitations of the model can be discussed. The model consists of a constant depth water layer covering a rigid sphere with no protruding land masses — "a water world". In practice, the water depth is not constant, with many deep trenches, sea-mounts, and land masses dispersed over the surface of the approximately spherical earth. The land masses in particular would break up the uniform film of water covering the sphere into distinct oceans. This alone is enough to introduce reflection/refraction effects unaccounted for in the model. The model does not take into account any dissipative mechanisms such as friction, and with the sphere being considered rigid, no elastic effects of the seabed are considered either. Elasticity is known to be significant [11,17], and Appendix B provides a detailed evaluation of its influence relative to compressibility and background density. Also, a more realistic model of the Earth system would require the rotation of the planet to be taken into account (Coriolis forces) along with the tidal forces generated by the moon and (to a lesser extent) the sun.

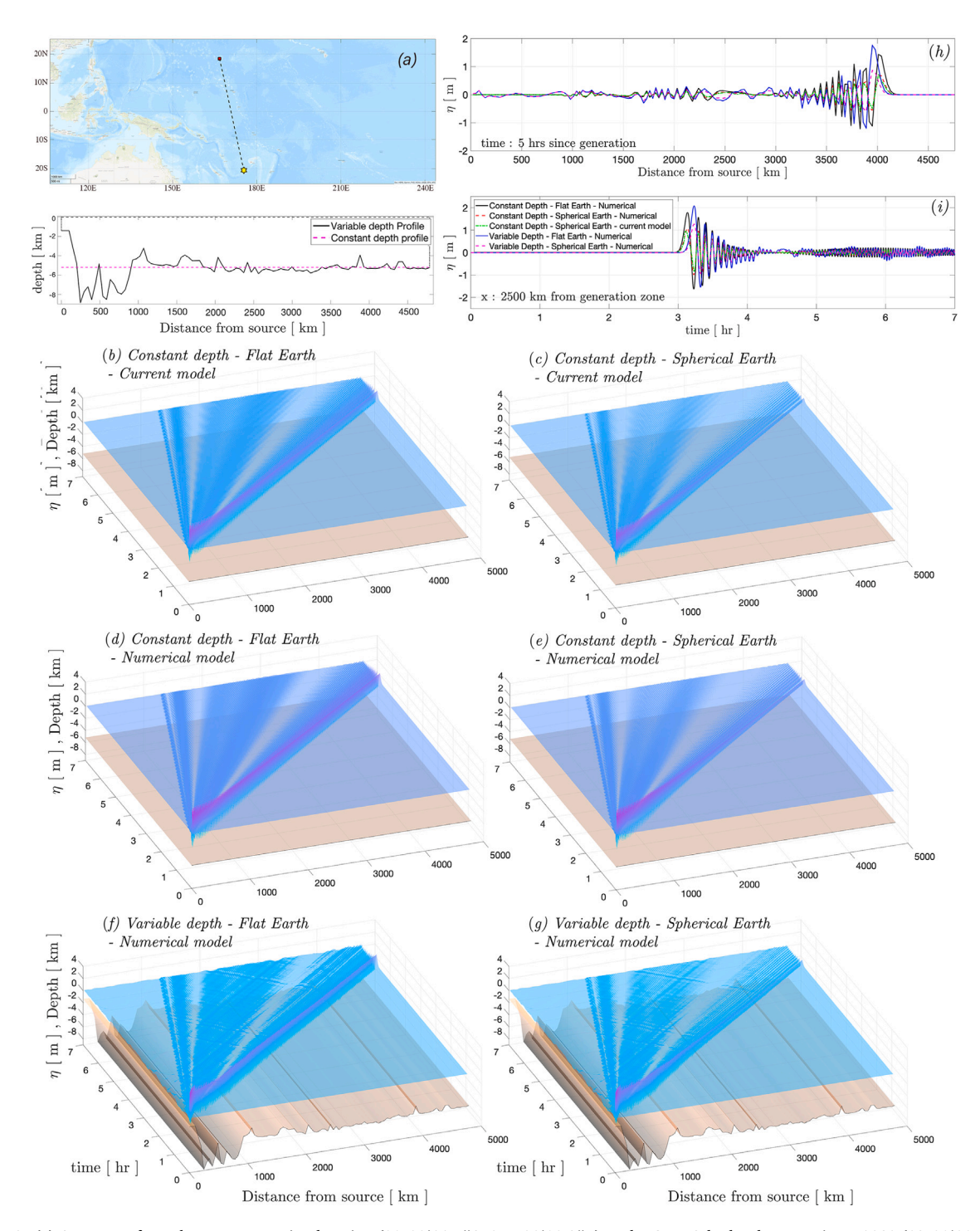


Fig. 6. (a) A transect from the HTHH eruption location (20°33′11.5″S, 175°23′02.8″E) to the CTBTO hydrophone station H11S1 (18°30′29.8″N, 166°42′01.0″E) spans approximately 4790 km. The panels illustrate results from a hypothetical event: a rapid 10 m sea surface elevation change over a 100 km width, initiated at the HTHH location. This is an idealised scenario and does not represent the actual eruption event. The average ocean depth along the transect is approximately 5200 m; (b) and (d) show sea surface elevation changes over 7 h under a flat Earth assumption with constant 5200 m depth—(b) from the current model (Section 3), (d) from a numerical model Appendix A; (c) and (e) are the same as (b) and (d), respectively, but with a spherical Earth assumption. (f) and (g) are similar to (d) and (e), respectively, but include realistic variable bathymetry. (h) presents time series of surface elevation along the transect 5 h after initiation for scenarios (b)–(g).(i) shows time series at a point 2500 km from the origin for the same scenarios. Panels (h) and (i) illustrate the impact of bathymetric variability and Earth geometry (flat vs. spherical) on wave arrival time and modulation.

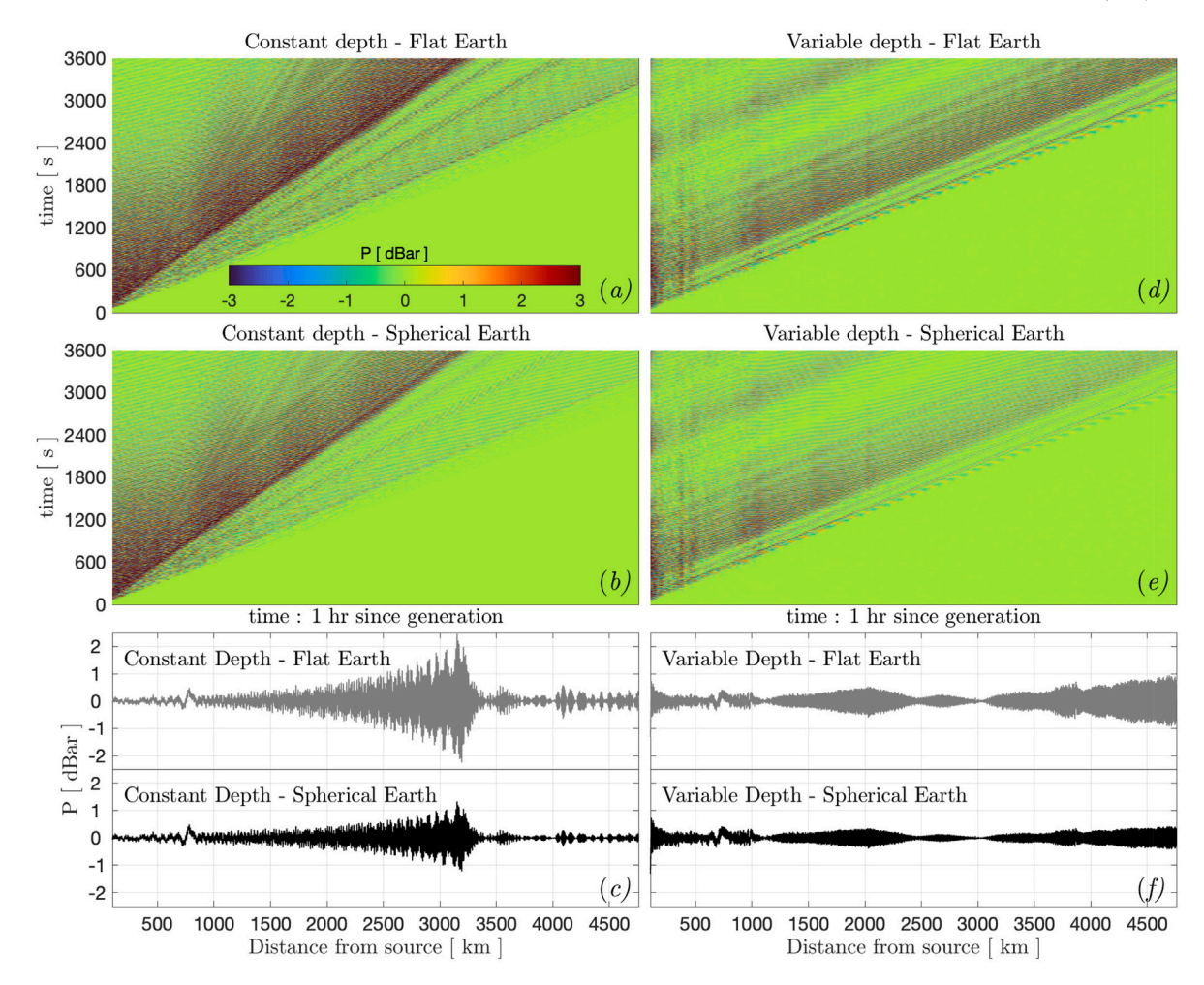


Fig. 7. Bottom pressure changes for the same scenario as in Fig. 6 are shown over time (1 h) and space: (a) under a flat Earth assumption with constant 5200 m depth; (b) the same as (a) but with a spherical Earth assumption; (d) similar to (a) but over realistic variable bathymetry; and (e) similar to (b) but with realistic bathymetry. Panels (c) and (f) show time series of bottom pressure changes along the transect 1 h after initiation, for scenarios (a) and (b) in (c), and for scenarios (d) and (e) in (f). Panels (c) and (f) highlight the effects of Earth curvature and bathymetry variability on acoustic signal characteristics.

4.3. Sensitivity to compressibility, variable bathymetry, and sound speed

We further investigated the properties of surface and acoustic gravity waves through detailed numerical modelling (see Appendix A for more details on the numerical scheme applied), considering both constant and variable water depth, and using both flat and spherical Earth assumptions. To create a scenario representative of a real-world application, we selected the location of the Hunga Tonga–Hunga Ha'apai (HTHH) eruption and a nearby hydrophone station, approximately 4700 km apart. It is important to note that this is a hypothetical scenario and does not replicate the actual 2022 HTHH event; rather, it uses the eruption site as the source location for idealised modelling purposes. The locations of the two points and the extracted transect are shown in Fig. 6a. The average ocean depth along this transect is approximately 5200 m.

The generated wave is initiated by an instantaneous sea bottom movement over a width of 100 km, lasting for 10 s, with a vertical velocity of 1 m/s. The model employed in these scenarios is based on the formulation presented in [18], Section 3, where a weakly compressible (first-order approximation of fluid density and pressure), inviscid, and irrotational fluid is considered. The sound speed can be specified explicitly or assumed to approach infinity to represent an incompressible fluid, and the depth profile can be variable. We conducted simulations under the following scenarios, using both flat assumptions, and applied the $\Theta(\theta)$ function to obtain a spherical correction:

- 1. Incompressible ocean over constant depth,
- 2. Incompressible ocean over variable depth,
- 3. Compressible ocean over constant depth,

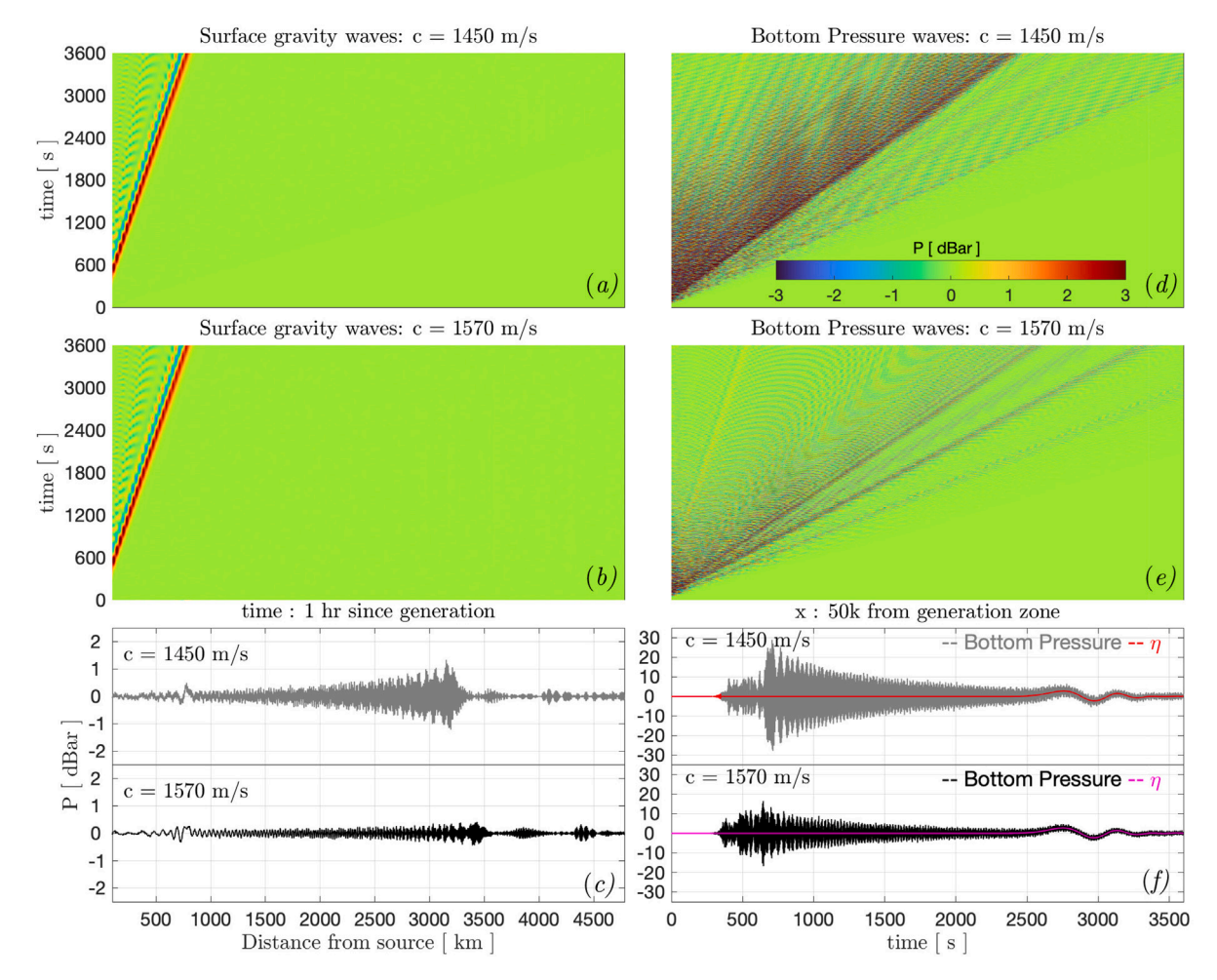


Fig. 8. Surface gravity waves and bottom pressure waves for different sound speeds along a constant-depth transect (5200 m) and with Spherical Earth assumption (using the $\Theta(\theta)$ function), as in Fig. 6: (a) surface gravity waves with sound speed c=1450 m/s, and (b) with c=1570 m/s; (d) bottom pressure waves with c=1450 m/s, and (e) with c=1570 m/s. Panel (c) shows time series of bottom pressure changes along the transect 1 h after initiation, comparing c=1450 m/s (grey line) and c=1570 m/s (black line). Panel (f) shows the time series of both bottom pressure (grey and black) and surface gravity waves (red and magenta) recorded 50 km away from the generation zone for. (For interpretation of the references to colour in this figure legend, the reader is referred to the web version of this article.)

- 4. Compressible ocean over variable depth,
- 5. Compressible ocean over constant depth with a sound speed of 1450 m/s,
- 6. Compressible ocean over constant depth with a sound speed of 1570 m/s.

First, the theoretical development presented in Section 3, illustrated in the second row of Fig. 6, is validated against the numerical experiments shown in the third row and described in Appendix A. This comparison assumes a flat bottom with an average depth of 5200 m along the transect, as shown in panel (a). Results are provided for both the flat Earth approximation (panels b and d) and the spherical Earth configuration (panels c and e). The flat bottom solution, derived from the analytical formulation, can be obtained rapidly which offers substantial computational advantages over resource-intensive numerical models. As such, it serves as a practical reference for evaluating the suitability of flat-bottom assumptions in operational applications. Following this initial validation, the flat bottom scenario is compared with the variable depth case (fourth row) to assess the impact of bathymetric complexity.

For Scenarios 1 and 2, the spatio-temporal evolution of surface waves in an incompressible ocean is analysed, as shown in Fig. 6. Panels (d) and (f) illustrate the effects of variable bathymetry, which modify both the structure and modulation of the wave field. Comparisons between the left-hand panels (b–f) and the corresponding right-hand panels (c–g) highlight the differences between flat and spherical Earth assumptions under both constant-depth (second and third rows) and variable-depth (bottom row) conditions. Panel (h) presents a snapshot of the surface waves 5 h after the simulation begins, integrating spatial patterns from panels (b) through (g). This snapshot reveals the influence of bathymetric variation on wave modulation, the damping effects introduced by Earth curvature, and the degree of agreement between constant and variable depth solutions, particularly within the range of

1500 km to 4500 km from the source. Finally, panel (i) shows the time series of surface elevation recorded 2500 km from the source, displaying notable differences in wave arrival time and amplitude. These results further highlight the importance of accounting for both bathymetry and Earth's geometry in accurate wave modelling.

Examining the transect shown in panel (a), the presence of irregular topography – including a shallow region near the source and a deep trench within the first 1000 km – led to variations in arrival time, following the depth-dependent phase speed relationship for an incompressible ocean over a rigid bottom, as illustrated in Fig. B.11.

Scenarios 3 and 4 are compared in Fig. 7, with a focus on the properties of bottom pressure acoustic gravity waves (AGWs). The left-hand side panels correspond to the constant depth case, while the right-hand side panels illustrate the effects of depth variability on AGW behaviour. The top panels present the results under a flat Earth assumption, whereas the middle panels show the results considering Earth curvature.

The bottom panels display a snapshot of the along-transect bottom pressure signal taken 1 h after the initiation of the simulation, with the left panel representing the constant depth case and the right panel showing the variable depth case. Notably, the inclusion of Earth curvature leads to a damping effect, where wave amplitudes gradually decrease as the waves propagate farther from the source. This attenuation is due to the geometric spreading of the wave energy over a curved surface, which is absent in flat Earth simulations.

In addition to the effects of Earth curvature, bottom variability significantly influences AGW characteristics. Variations in bathymetry modify the modulation patterns of the propagating waves and shift the dominant (carrying) frequencies. In the case of a flat bottom, the wave modes and frequency content follow the well-defined dispersion relationship for mode n given by Eq. (4.58), whereas over a variable bottom, the governing relationships become more complex and spatially dependent. Bathymetric irregularities introduce local changes in phase speed, causing partial reflections and refractions of the wave energy. These processes lead to interference patterns, spectral broadening, and complex waveform structures along the transect. Consequently, the bottom variability plays a key role in shaping the spectral and temporal properties of the bottom pressure signals observed at distant locations.

$$f_n = \frac{(2n-1)c}{4h}, \ n = 1, 2, \dots$$
 (4.58)

Overall, the comparison highlights that both Earth curvature and bathymetric variability play critical roles in shaping AGW properties. Neglecting either effect would result in notable inaccuracies when predicting the propagation, amplitude, and frequency content of acoustic gravity waves over oceanic scales.

Comparing scenarios 1–4, particularly for surface gravity waves, highlights the influence of ocean compressibility on phase speed reduction. This reduction in phase speed (~4 min over 4700 km length scale), in turn, alters the surface wave modulation patterns and shifts the peak arrival times, consistent with the behaviour discussed earlier.

Finally, to investigate the impact of sound speed on wave propagation, we considered two extreme values representative of oceanic conditions, where the sound speed can vary spatially due to temperature and salinity, particularly with latitude. Specifically, we selected sound speeds of 1450 m/s and 1570 m/s, corresponding to cold and warm water extremes, respectively. We performed simulations using a compressible ocean model over a flat bottom, keeping all other parameters the same.

The results are shown in Fig. 8. Panels (a) and (b) present the surface gravity wave responses for sound speeds of 1450 m/s and 1570 m/s, respectively. The comparison indicates that changes in sound speed have a negligible effect on surface waves, with only a slight reduction in phase speed observed — approximately a 0.2% difference. This marginal effect is consistent with the fact that surface gravity wave dynamics are primarily governed by gravity and depth, with compressibility effects being secondary at these scales, and become important in transoceanic scale simulations.

In contrast, the bottom pressure signals exhibit a more noticeable sensitivity to sound speed variation. Panels (d) and (e) show the bottom pressure fields for the two cases, revealing changes in both amplitude and waveform structure. A closer inspection, provided in panel (c), shows a snapshot of the spatial distribution of bottom pressure one hour after simulation initiation, where phase lags and amplitude differences between the two cases become apparent.

Panel (f) further illustrates these differences by showing time series records of both long gravity waves and bottom pressure signals, taken 50 km away from the generation zone. The results highlight a larger amplitude in the bottom pressure signal for the lower sound speed case (1450 m/s), whereas the surface gravity wave signals remain nearly identical between the two sound speed scenarios (red and magenta lines in panel f).

It is important to note that, in reality, ocean sound speed varies continuously with both depth (vertically) and location (horizontally) due to changes in salinity and temperature. While this study focused on two extreme cases with constant sound speeds to highlight potential impacts in idealised scenarios, the natural horizontal and vertical variability of sound speed remains a critical factor.

4.4. Hunga Tonga-Hunga Ha'apai eruption

The axially symmetric, cylindrical rupture model developed in [9], coupled with the global extent of the results obtained in this paper suggest a qualitative comparison may be made with the HTHH eruption studied in [10]. The HTHH volcanic eruption of 15th January 2022 was one of the largest of the last 30 years and generated concentric, propagating atmospheric acoustic–gravity waves that radiated outwards globally from the source.

The HTHH eruption was modelled in [10] as a moving atmospheric source, coupled to the ocean surface, able to transfer energy into the ocean via a triad resonance mechanism [10]. For comparison purposes, we regard the volcanic eruption as an uplifting

Table 2Constants and parameters used in the HTHH qualitative model.

Constant	Description	Value
g	Acceleration due to gravity	9.81 m s ⁻²
r_e	Radius of earth	6371 km
R_c	Radius of cylindrical rupture	1100 m
R_0	Radius of inner region	120 000 m
ρ_a	Air density	1.2 kg m^{-3}
c	Speed of sound in air	343 m s ⁻¹
W_0	Uplift velocity	400 m s^{-1}
n	Acoustic mode	1
τ	Uplift duration	0.2 s

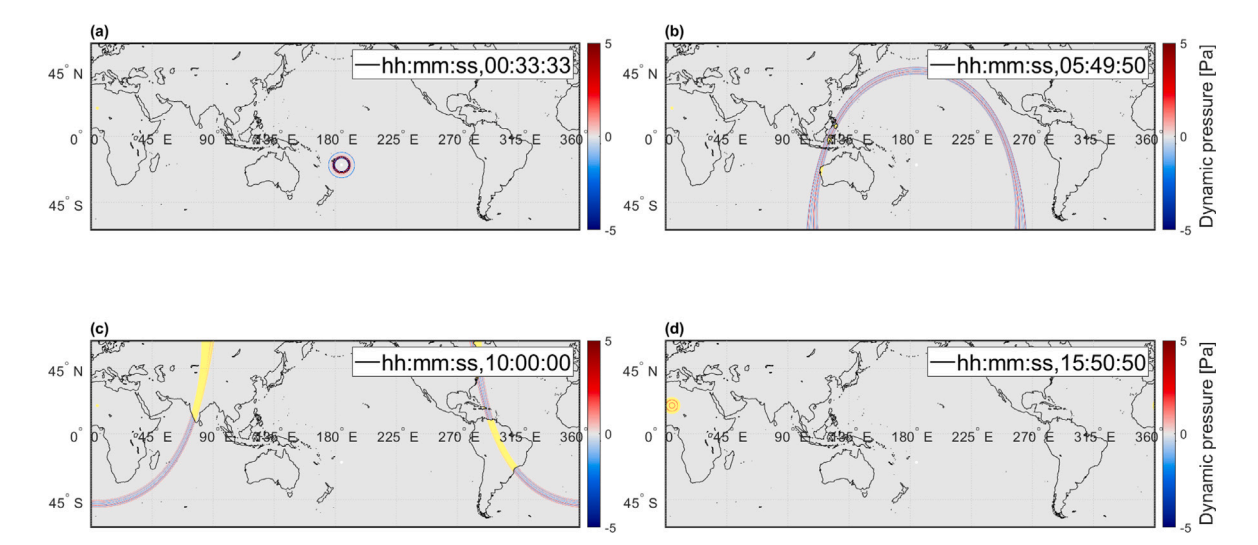


Fig. 9. Progression of acoustic–gravity waves generated by point source model of the HTHH 2022 eruption. (a) Circular wavefront shortly after the eruption, (b) Wavefront has now travelled almost halfway around the world. This is just before maximum defocusing is achieved. (c) Just after maximum defocusing, the wavefront is now past the halfway point and is beginning to focus again. (d) The wavefront has reached its antipodal point over North Africa and has focused here.

cylinder moving in a low-density fluid (the atmosphere). The parameters used for the comparison are those found in Figure 7 of Omira et al. [10], and reproduced in Table 2. The explosive nature of the event is reflected in the supersonic uplift velocity and short duration. Our model is that of a point source, rather than a moving source, as in [10], and no coupling (resonance) with the liquid layer is considered. These constraints limit our comparison to be qualitative only. Fig. 9 shows the progression of the acoustic–gravity wavefront at four distinct times. Fig. 9(a) is just after the eruption, and shows the circular wave-front of the acoustic–gravity waves as pictured in the satellite imagery of Figure 1 [10]. Fig. 9(b) and (c) represent the acoustic–gravity wave's progression just before, and just after, the point of maximum defocusing respectively. Fig. 9(d) has the acoustic–gravity wave focusing at its antipodal point lying over North Africa. The defocusing is apparent in the less intense acoustic–gravity wave in Fig. 9(b) and (c) when compared to Fig. 9(a) and (d) — see supplementary video.

4.5. Rectangular fault source

In this section, we apply the Θ function to a rectangular fault. Although the earlier derivation pertains to a cylindrical source, at far-field distances, the curvature of a wavefront segment – be it tsunami or acoustic–gravity waves – becomes negligible. This allows the curvature correction to be applicable to arbitrary wavefronts. To illustrate the effect of Earth's curvature on the dispersion of the leading acoustic–gravity wave amplitude envelope $|A_1|$, we consider a fault measuring 40 km in width and 800 km in length, undergoing vertical motion at 0.1 m/s for 10 s, following the example discussed by Mei and Kadri [2]. The solution for A_1 can be found in equation (5.10) of their work. Fig. 10 presents the spatial evolution of the leading acoustic mode's envelope for a flat Earth model (a) and a spherical Earth model (b). At a distance of 8000 km, the amplitude experiences an approximate 60% reduction due to Earth's curvature (c).

The methodology presented herein offers a computationally efficient correction for long-range wave propagation calculations, accounting for Earth's curvature. This approach is particularly valuable for real-time applications, such as tsunami assessment based on acoustic signals [5], where rapid analysis is crucial and waiting for more detailed, computationally intensive models is not feasible. However, it is essential to apply these findings judiciously and with a comprehensive understanding of their limitations.

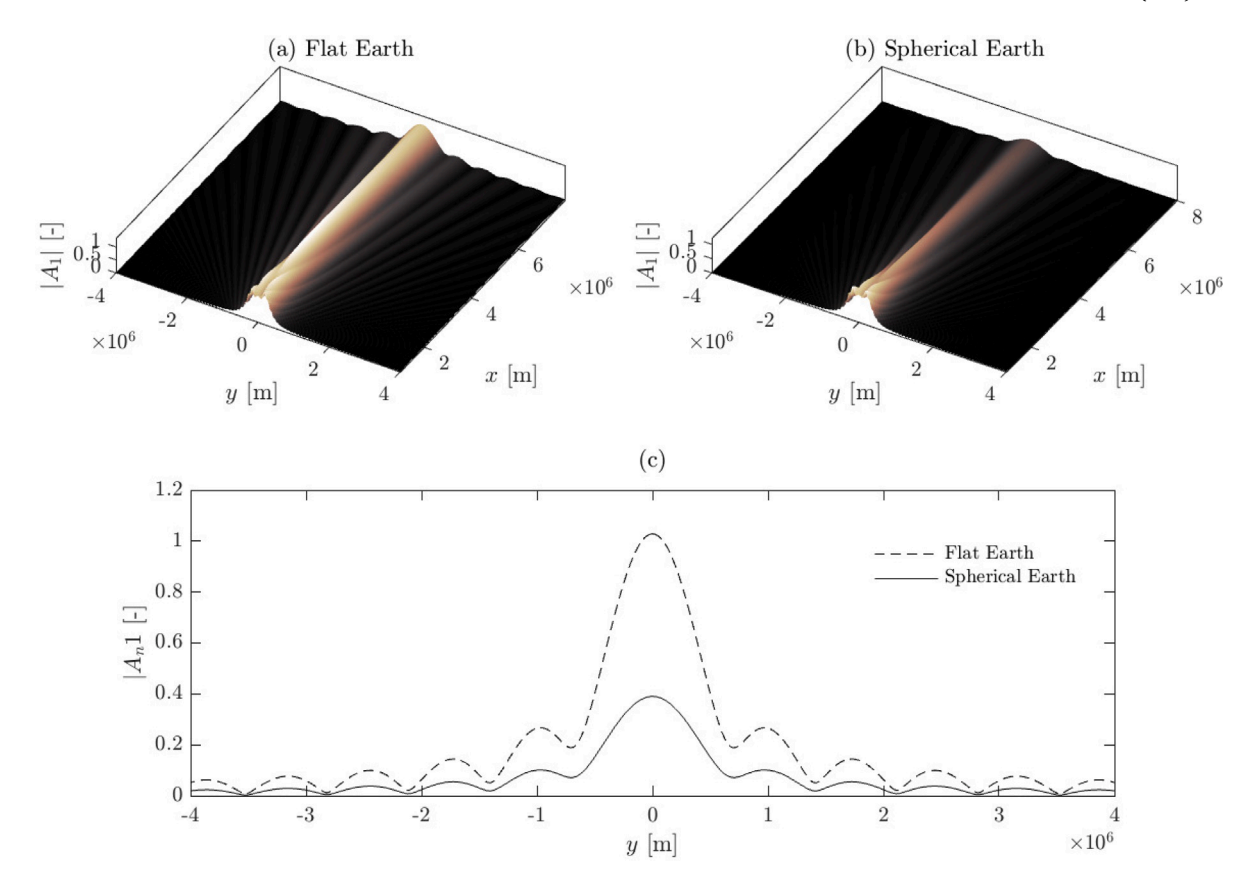


Fig. 10. Comparison of the amplitude envelope of the leading acoustic mode $|A_1|$ in the x-y plane: (a) flat Earth model; (b) spherical Earth model. (c) Far-field comparison of acoustic amplitude envelopes at x = 8000 km: flat Earth (dashed line) versus spherical Earth (solid line).

In scenarios where bathymetric variations are significant, additional corrections may be necessary. For instance, employing Green's function methods or other energy conservation techniques can help compensate for localised changes due to bathymetry, enhancing the accuracy of the model in complex terrains.

The work presented in this paper could be extended in a number of ways. One of which could be the development of a computational fluid dynamics (CFD) validation model. The assumptions of constant depth, solid and rigid sphere, no tides, and no rotation discussed earlier could make validation using recorded data difficult. Experiments using water tanks are also of no help due to the global scale and curvature involved. Once the CFD model had been set up, and the focusing/defocusing effects verified, then other assumptions could be investigated. Elasticity, tides, rotation (Coriolis), and dissipation would all be candidates for further study. Also, the small correction due to Earth's geometry being closer to an oblate spheroid rather than a perfect sphere could be included.

5. Conclusions

In this work we present an analytical framework to account for Earth's curvature in models of long-range tsunami and acoustic-gravity wave propagation, addressing a key limitation of near-field models that rely on Cartesian or cylindrical coordinates. By matching a near-field cylindrical solution to a far-field spherical solution through a two-scale asymptotic approach, we derived the function $\Theta(\theta)$, which is a solution to Legendre's equation, that analytically captures the geometrical defocusing of wave amplitudes as they travel toward the equator and their subsequent refocusing toward the antipode. The result is a simple, direct, computationally efficient correction factor that links the source dynamics to far-field wave evolution using only global geometric considerations. This correction can be implemented in operational models for large-scale applications (due to its low computational cost), offering an alternative to fully numerical methods that are significantly more resource-intensive — which resonates with recent findings on the significance of simpler models and how they can outperform deep learning in climate prediction [19]. Importantly, we also quantified this curvature-induced effect in relation to other physical processes with comparable influence, including ocean compressibility, seabed elasticity, background density structure, bathymetric variability, and sound speed gradients.

The validity and practicality of the proposed correction were tested against a range of physical parameters. In an idealised constant-depth scenario, the analytical model's prediction of amplitude decay was validated against numerical simulations, revealing a pronounced defocusing effect at distances approaching 10,000 km (Fig. 5). The investigation was then extended to more complex cases, showing that while Earth's curvature is a dominant factor in far-field amplitude decay, causing approximately 60% reduction for a rectangular fault source at 8000 km (Fig. 10), other factors play important roles. In particular, ocean compressibility, seabed elasticity, and background density introduce significant, period-dependent reductions in wave phase speed, while variable bathymetry primarily affects waveform modulation and arrival time (Figs. 6, 7, B.11, B.12). Furthermore, our analysis demonstrated that variations in sound speed (from 1450 to 1570 m/s) have a negligible influence on surface gravity waves but a more noticeable effect on bottom pressure amplitudes and phase shifts (Fig. 8).

Finally, the model qualitatively reproduced the global propagation pattern of atmospheric waves from the 2022 Hunga Tonga—Hunga Ha'apai eruption, including the observed defocusing and antipodal focusing behaviour (Fig. 9). While the theoretical framework is based on simplified assumptions – such as constant depth, uniform background structure, and idealised wave sources – our comparative analysis highlights the limitations of these assumptions and identifies conditions under which other physical effects may become more influential than Earth's curvature. For instance, bathymetric variability can significantly affect wave modulation, while for long-period waves, processes such as ocean compressibility, seabed elasticity, and background density gradients can alter phase speed — effects that may outweigh geometric spreading. Nevertheless, this work provides not only a robust theoretical foundation for understanding geometrical spreading on a sphere, but also a practical, first-order correction that has been quantitatively assessed relative to other key physical processes. As such, it represents a valuable component for integration into real-time tsunami assessment systems, where both computational efficiency and physical accuracy are essential.

CRediT authorship contribution statement

Byron Williams: Writing – original draft, Investigation, Formal analysis. **Ali Abdolali:** Writing – review & editing, Validation, Formal analysis. **Usama Kadri:** Writing – review & editing, Supervision, Formal analysis, Conceptualization.

Declaration of competing interest

The authors declare that they have no known competing financial interests or personal relationships that could have appeared to influence the work reported in this paper.

Acknowledgement

Ali Abdolali gratefully acknowledges the support of the USACE, USA under Program Element 0601102 A [Project AB2].

Appendix A. Numerical model

The numerical model is based on the governing equation for the velocity potential $\varphi(x, y, z, t)$:

$$\frac{\partial^2 \varphi}{\partial t^2} - c^2 \left(\nabla_h^2 \varphi - \varphi_{zz} \right) = 0, \quad -h \le z \le 0 \tag{A.1}$$

Here, c is the sound speed, and h is the local water depth, which may vary spatially. The operator ∇_h represents the horizontal gradient, and subscripts on dependent variables denote partial derivatives. The system is subject to combined kinematic and dynamic boundary conditions applied at the free surface,

$$\frac{\partial^2 \varphi}{\partial t^2} + g\varphi_z = 0, \quad z = 0 \tag{A.2}$$

where g is the gravitational acceleration, and the impermeable (but possibly moving) bottom, z = -h:

$$\phi_z(x,t) = \begin{cases} \frac{\zeta_0}{\tau}, & 0 \le t \le \tau, \quad 0 \le x \le b\\ 0, & t > \tau \text{ or } x > b, \end{cases}$$

$$(A.3)$$

where ζ_0 is the total residual bottom displacement, τ is the total duration of the motion, and b is the displacement length. Additionally, the wave field must satisfy an outgoing radiation condition at large distances. To enforce this, we apply the Sommerfeld radiation condition along an artificial boundary placed sufficiently far from the wave source region.

We employed the finite element solver in COMSOL MULTIPHYSICS [20], using unstructured triangular meshes. The model geometry is imported from a transect extracted using bathymetric data from the GEBCO Digital Elevation Model (DEM) [21]. Time integration is performed using an implicit scheme based on the generalised-Alpha method, which ensures numerical stability and convergence over variable-resolution meshes. Full details are provided in [18].

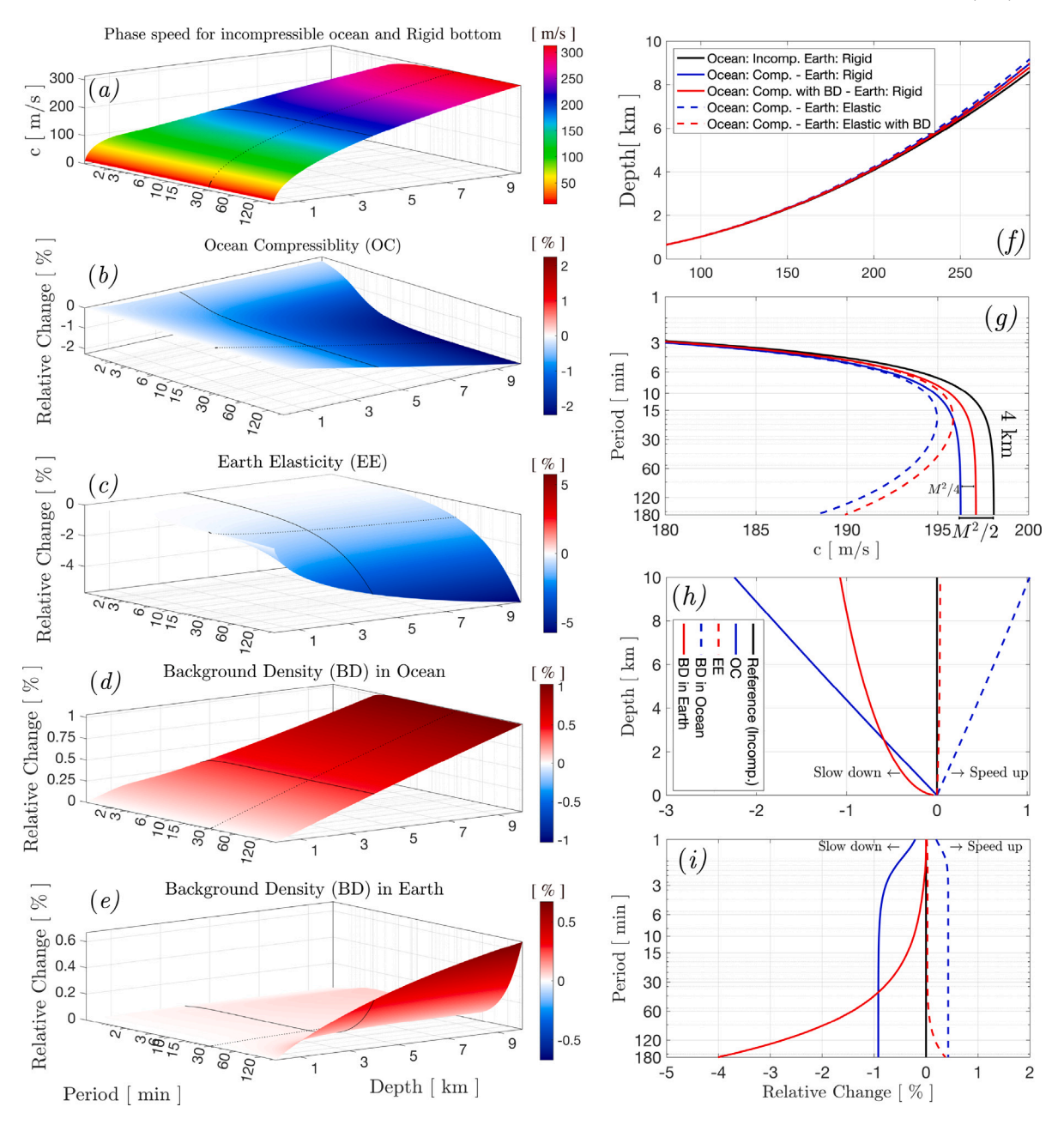


Fig. B.11. Left-hand side panels: (a) Phase speed of surface waves as a function of water depth (0–10 km) and wave period (1 min to 3 h) from an incompressible ocean and rigid bottom dispersion relation as benchmark. Panels (b) through (e) show the relative changes in phase speed due to individual physical effects: (b) ocean compressibility (OC), (c) Earth's elasticity (EE), (d) background density (BD) in the ocean, and (e) background density in the solid Earth. Right-hand side panels provide a detailed zoom-in view: Panel (f) shows phase speed for a fixed wave period of 30 min across depths from 0 to 10 km, and panel (h) presents the corresponding relative changes in phase speed due to ocean compressibility, Earth elasticity, and background density in both ocean and Earth; (g) phase speed at a fixed water depth of 4 km across wave periods from 1 min to 3 h; (g) the corresponding relative change in phase speed for panel (i), highlighting the impact of various physical factors. Notably, the effects of ocean compressibility and background ocean density approach asymptotic behaviours of $-M^2/2$ and $M^2/4$, respectively, where $M = \sqrt{gh/c}$ is a Mach number based on the linear long-wave speed for an incompressible surface gravity wave.

Appendix B. Ocean compressibility, seabed elasticity, & background density

To evaluate the influence of ocean compressibility, Earth's elasticity, and background density ($g\phi_z$ terms) on wave propagation, we conducted a series of analyses that quantify each factor's relative contribution across a broad spectrum of wave types and

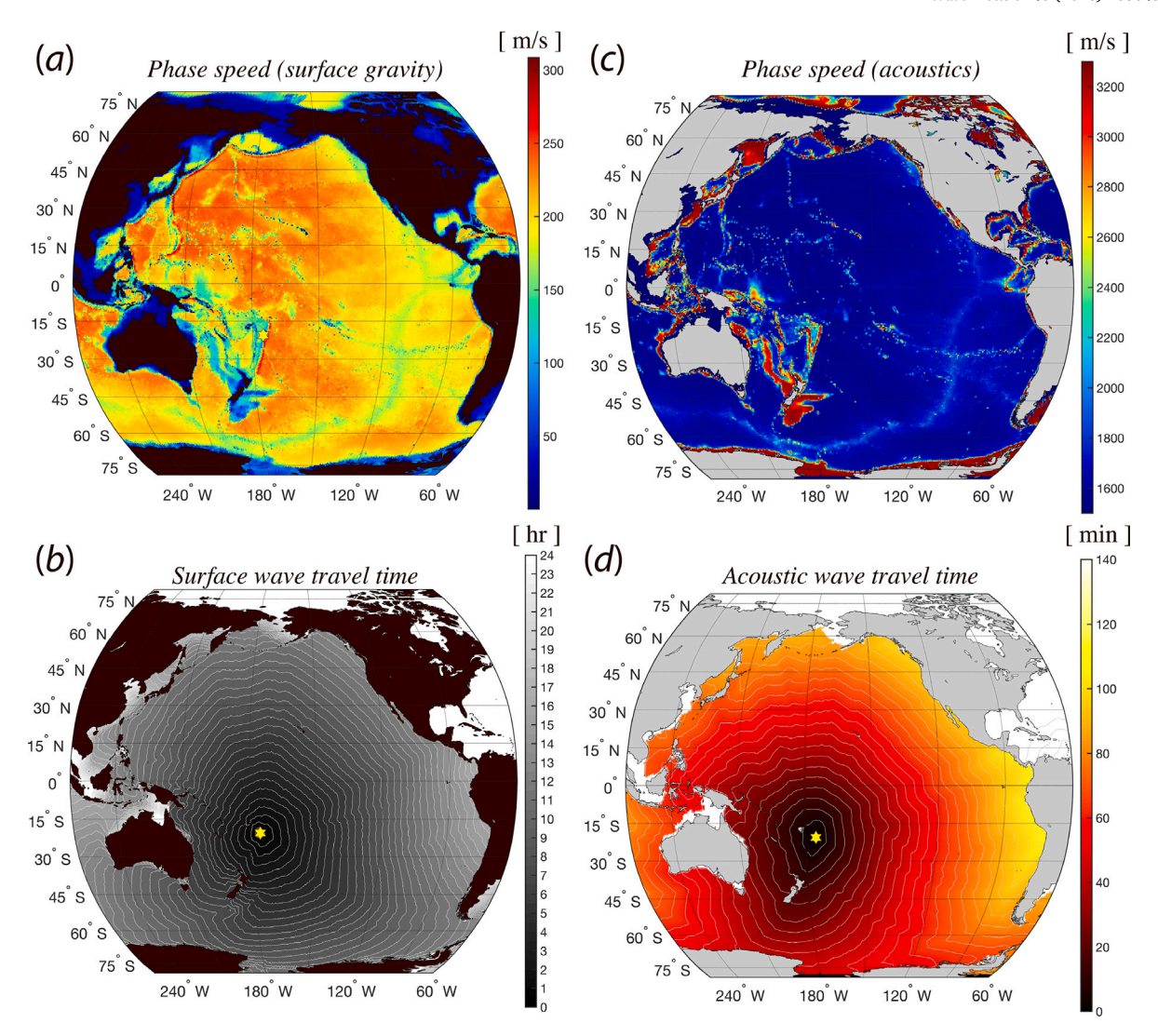


Fig. B.12. Phase speed of (a) surface gravity waves and (b) acoustic waves, derived using the dispersion relation for a compressible ocean overlying an elastic half-space, incorporating background density profiles for both the ocean and the solid Earth. Arrival times for (c) surface gravity waves are shown with 30-min contours, and (d) acoustic waves with 300-s contours. The surface wavefronts are computed for a 30-minute-period wave, while acoustic propagation is modelled for a 5-second-period signal, both using the solution of dispersion relation given by Eq. 2 of Abdolali et al. [11]. The source location is marked by a yellow star, corresponding to the HTHH eruption. (For interpretation of the references to colour in this figure legend, the reader is referred to the web version of this article.)

conditions. For calculating wave travel times over long distances on a global spherical domain, we employed a shortest-path algorithm based on Dijkstra's method [5]. This algorithm accounts for the propagation of two distinct wave types generated by a single source: (1) surface gravity waves and (2) acoustic–gravity waves. To determine the phase speeds of these waves, we solved the dispersion relation for a compressible ocean overlaying an elastic half-space Earth, incorporating background density in both the ocean and Earth's interior. This comprehensive approach ensures that the model accurately reflects the physical characteristics influencing wave propagation.

Fig. B.11 illustrates the resulting phase speeds for varying water depths (0 to 10 km) and wave periods ranging from 15 min to 3 h, encompassing the typical range of tsunami wave periods. Phase speeds are derived using the dispersion relation solutions from [11], and relative changes are computed to isolate the effects of individual physical parameters. Panel (a) in Fig. B.11 presents the benchmark solution based on the classical dispersion relation for an incompressible ocean over a rigid seafloor. This serves as a reference case and corresponds with results produced by conventional numerical models. Panels (b) through (e) display the relative changes in phase speed arising from ocean compressibility, Earth's elasticity, and background density. The results demonstrate a noticeable reduction in wave speed due to compressibility and elasticity, particularly at longer wave periods, while the inclusion of background density leads to a slight increase in phase speed. In the shallow water limit, ocean compressibility reduces the phase

speed by approximately $M^2/2$, where $M = \sqrt{gh/c}$ is the acoustic Mach number. Conversely, the inclusion of the gravitational potential term $g\phi_z$ leads to a phase speed increase of approximately $M^2/4$ in shallow water. These effects, when combined with Earth curvature, result in a significant change in propagation speed (slowdown) and arrival time at transoceanic scales [11,22].

A more detailed view is provided on the right-hand side of Fig. B.11, illustrating the variation in relative phase speed for two scenarios: (1) a fixed average water depth of 4km across a range of wave periods, and (2) waves with a 30 min period over water depths ranging from 0 to 10 km.

The Earth and ocean parameters employed in this study are as follows: water density ($\rho_w = 1020 \text{ kg/m}^3$), Earth density ($\rho_e = 2750 \text{ kg/m}^3$), sound speed in water (c = 1500 m/s), shear wave speed in Earth ($c_s = 2750 \text{ m/s}$), and compressional wave speed in Earth ($c_p = 6300 \text{ m/s}$). These values represent standard conditions for a compressible ocean overlying an elastic Earth and are essential for solving the dispersion relation governing both surface and acoustic–gravity wave propagation.

Once the solutions for varying depths are computed, Dijkstra's algorithm is applied to calculate the arrival times of wave fronts, as shown in Fig. B.12. Panel (a) displays the phase speeds obtained by solving the dispersion relation, including ocean compressibility, Earth's elasticity, and background density (Eq. 2; [11]), for both the surface wave and the first acoustic mode, incorporating all relevant parameters. Panel (b) shows the computed arrival times of the surface gravity wavefront, while panel (c) presents the phase speed of the first acoustic mode. Finally, panel (d) illustrates the arrival times of the acoustic wavefront.

Appendix C. Supplementary data

Supplementary material related to this article can be found online at https://doi.org/10.1016/j.wavemoti.2025.103643.

Data availability

Data will be made available on request.

References

- [1] T. Yamamoto, Gravity waves and acoustic waves generated by submarine earthquakes, Int. J. Soil Dyn. Earthq. Eng. (ISSN: 02617277) 1 (2) (1982) 75–82, http://dx.doi.org/10.1016/0261-7277(82)90016-X. URL http://linkinghub.elsevier.com/retrieve/pii/026172778290016X.
- [2] C.C. Mei, U. Kadri, Sound signals of tsunamis from a slender fault, J. Fluid Mech. 836 (2018) 352–373, http://dx.doi.org/10.1017/jfm.2017.811, ISSN 0022-1120, 1469-7645, URL https://www.cambridge.org/core/product/identifier/S0022112017008114/type/journal_article.
- [3] B. Williams, U. Kadri, A. Abdolali, Acoustic-gravity waves from multi-fault rupture, J. Fluid Mech. (ISSN: 1469-7645) 915 (2021) A108-undefined, http://dx.doi.org/10.1017/jfm.2021.101, URL https://www.cambridge.org/core/article/acousticgravity-waves-from-multifault-rupture/EBEB7BDE871BC4833A91D54263D2740D.
- [4] B. Gomez, U. Kadri, Near real-time calculation of submarine fault properties using an inverse model of acoustic signals, Appl. Ocean Res. (ISSN: 0141-1187) 109 (2021) 102557, http://dx.doi.org/10.1016/j.apor.2021.102557, URL https://www.sciencedirect.com/science/article/pii/S0141118721000341.
- [5] U. Kadri, A. Abdolali, M. Filimonov, GREAT v1.0: Global real-time early assessment of tsunamis, Geosci. Model. Dev. 18 (11) (2025) 3487–3507, http://dx.doi.org/10.5194/gmd-18-3487-2025, URL https://gmd.copernicus.org/articles/18/3487/2025/.
- [6] M. Stiassnie, Tsunamis and acoustic-gravity waves from underwater earthquakes, J. Engrg. Math. 67 (1–2) (2010) 23–32, http://dx.doi.org/10.1007/s10665-009-9323-x, ISSN 0022-0833, 1573-2703, URL http://link.springer.com/10.1007/s10665-009-9323-x.
- [7] E. Eyov, A. Klar, U. Kadri, M. Stiassnie, Progressive waves in a compressible-ocean with an elastic bottom, Wave Motion (ISSN: 01652125) 50 (5) (2013) 929–939. http://dx.doi.org/10.1016/j.wavemoti.2013.03.003. URL http://linkinghub.elsevier.com/retrieve/pii/S016521251300053X.
- [8] A. Dziewonshi, D. Anderson, Preliminary earth reference model, Phys. Earth Planet. Inter. 25 (1981) 297–356.
- [9] G. Hendin, M. Stiassnie, Tsunami and acoustic-gravity waves in water of constant depth, Phys. Fluids 25 (8) (2013) 086103, http://dx.doi.org/10.1063/1.4817996, ISSN 1070-6631, 1089-7666, URL http://aip.scitation.org/doi/10.1063/1.4817996.
- [10] R. Omira, R.S. Ramalho, J. Kim, P.J. González, U. Kadri, J.M. Miranda, F. Carrilho, M.A. Baptista, Global Tonga tsunami explained by a fast-moving atmospheric source, Nat. 609 (7928) (2022) 734–740, http://dx.doi.org/10.1038/s41586-022-04926-4, ISSN 0028-0836, 1476-4687, URL https://www.nature.com/articles/s41586-022-04926-4.
- [11] A. Abdolali, U. Kadri, J.T. Kirby, Effect of water compressibility, sea-floor elasticity, and field gravitational potential on tsunami phase speed, Sci. Rep. (ISSN: 2045-2322) 9 (1) (2019) 16874, http://dx.doi.org/10.1038/s41598-019-52475-0, URL http://www.nature.com/articles/s41598-019-52475-0.
- [12] C.C. Mei, M. Stiassnie, D.K.-P. Yue, Theory and Applications of Ocean Surface Waves, World Scientific, New Jersey, 2009, ISBN 981-256-157-9 978-981-256-157-2 981-256-159-5 978-981-256-159-6 981-238-894-X 978-981-238-894-0.
- [13] P. Moon, D.E. Spencer, Field Theory Handbook: Including Coordinate Systems, Differential Equations and Their Solutions, Springer Science & Business Media, ISBN: 978-3-642-83243-7, 1961, Google-Books-ID: O3TpCAAAQBAJ.
- [14] F.W.J. Olver (Ed.), NIST Handbook of Mathematical Functions, Cambridge University Press, NIST, Cambridge; New York, 2010, ISBN 978-0-521-19225-5 978-0-521-14063-8. OCLC: ocn502037224.
- [15] G. Hendin, Tsunami and Acoustic-Gravity Waves in Water of Constant Depth (Ph.D. thesis), (Technion, Israel Institute of Technology, 2013, p. 121, 2013.
- [16] G. Szegö, Orthogonal polynomials, American Mathematical Society Colloquium Publications, American Mathematical Society, ISBN: 978-0-8218-8952-7, 1959, Number v. 23, URL https://books.google.co.uk/books?id=3hcW8HBh7gsC.
- [17] U. Kadri, Effect of sea-bottom elasticity on the propagation of acoustic–gravity waves from impacting objects, Sci. Rep. (ISSN: 2045-2322) 9 (1) (2019) 912, http://dx.doi.org/10.1038/s41598-018-37626-z, URL http://www.nature.com/articles/s41598-018-37626-z.
- [18] A. Abdolali, C. Cecioni, G. Bellotti, J.T. Kirby, Hydro-acoustic and tsunami waves generated by the 2012 Haida Gwaii earthquake: Modeling and in situ measurements, J. Geophys. Res.: Ocean. 120 (2) (2015) 958–971, http://dx.doi.org/10.1002/2014JC010385, URL https://agupubs.onlinelibrary.wiley.com/doi/abs/10.1002/2014JC010385.
- [19] B. Lütjens, R. Ferrari, D. Watson-Parris, N.E. Selin, The impact of internal variability on benchmarking deep learning climate emulators, J. Adv. Model. Earth Syst. 17 (8) (2025) e2024MS004619, http://dx.doi.org/10.1029/2024MS004619, URL https://agupubs.onlinelibrary.wiley.com/doi/abs/10.1029/2024MS004619, e2024MS004619 2024MS004619.
- [20] COMSOL Incorpration, COMSOL multiphysics, 2024, URL https://www.comsol.com/products/multiphysics/.
- [21] GEBCO Compilation Group, GEBCO 2023 grid, 2023, https://www.gebco.net/data_and_products/gridded_bathymetry_data/.
- [22] A. Abdolali, J.T. Kirby, Role of compressibility on tsunami propagation, J. Geophys. Res.: Ocean. (ISSN: 21699275) 122 (12) (2017) 9780–9794, http://dx.doi.org/10.1002/2017JC013054, URL http://doi.wiley.com/10.1002/2017JC013054.